RESEARCH ARTICLE

WILEY

Dynamic brittle fracture with eigenerosion enhanced material point method

Kun Zhang[1] | **Shui-Long Shen[2,3]** | **Annan Zhou[3]**

[1]Department of Civil Engineering, School of Naval Architecture, Ocean, and Civil Engineering, Shanghai Jiao Tong University, Shanghai, China

[2]Key Laboratory of Intelligent Manufacturing Technology, Ministry of Education, Department of Civil and Environmental Engineering, College of Engineering, Shantou University, Shantou, China

[3]Civil and Infrastructure Discipline, School of Engineering, Royal Melbourne Institute of Technology, Melbourne, Victoria, Australia

Correspondence
Shui-Long Shen, College of Engineering, Shantou University, Shantou, Guangdong 515063, China.
Email: shensl@stu.edu.cn and shuilong.shen@rmit.edu.au

Funding information
Research Funding of Shantou University for New Faculty Member, Grant/Award Number: NTF19024-2019

Summary

This article proposes an approach to resolve the dynamic fracture of brittle materials by incorporating eigenerosion into the material point method (MPM) framework. The eigenerosion approach links the crack propagation to energy conservation based on the variational theory of fracture mechanics. This idea closely resembles the conventional treatment for the phase-field method. The major difference is that the effective energy release rate of each particle that controls the crack propagation is only calculated within its neighborhood domain for the eigenerosion approach. Because evaluation of the material's fracture behavior can be decoupled from the governing equations as a separate solution step, the eigenerosion scheme allows straightforward implementation into any standard MPM solver with minor modifications. In addition, a phantom-node method is employed to handle the preexisting crack. With these settings, the proposed model can capture complex fracture behaviors. Several representative benchmark tests demonstrate the efficiency and validity of the proposed model.

KEYWORDS

brittle fracture, eigenerosion approach, material point method, phantom-node method

1 | INTRODUCTION

Damage pertinent to the dynamic fracture in engineering materials and structures is ubiquitous to everyday life, but the underlying mechanisms are not simple. In order to understand the mechanisms of fracture processes and prevent fracture-induced failure, physically based numerical simulations are indispensable. Consequently, numerous fracture models have been developed. Among these, models based on Griffith's theory[1] are particularly favored as they describe crack nucleation and propagation from the perspective of energy balance that can be generalized to various situations. Within the framework of generalized Griffith's theory, fracture of solids is treated using either continuous (smeared) or discontinuous (discrete) approaches.

The most commonly used discontinuous approaches include the cracking node method,[2] the embedded discontinuous method,[3,4] the extended finite element method (XFEM),[5-7] and the cohesive zone method.[8-10] These methods allow the displacement field to be discontinuous across the cracked surfaces and model fracture explicitly either

by separating nodal points in a mesh or by altering the shape functions near crack tips. Although they show considerable success in obtaining high accuracy of the displacement and stress fields[11] when dealing with fracture problems, discontinuous approaches need to track the evolution of complex crack paths using algorithms. This requires well-designed techniques and has proven to be a tedious task,[12,13] particularly for problems involving multiple crack patterns.

By contrast with a discontinuous approach, a continuous approach models crack using a smear-like method, where displacements are assumed to remain continuous around the cracked surfaces, and instead, the mechanical properties of the cracked parts are weakened to consider the effects of fracture.[14] Within this set of methods, the fracture can be approximated either locally or nonlocally. In the former, the fracture is often tracked by calculating the ratio of the current local stress to a preset maximal stress.[15,16] By contrast, in the latter, the fracture is usually represented by a scalar damage field, like a phase field.[12,17,18] One advantage of the local type method is its higher efficiency in calculating the crack trajectory; it is, however, difficult to capture topologically complex fractures such as branching and intersections.[14] On the contrary, the nonlocal type method exhibits considerable potential in producing such multiple modes of fracture.

As one of the representative nonlocal type continuous approaches, the phase-field method describes the crack by a field variable ranging from 0 to 1, which can smoothen discontinuities caused by the crack. At present, there are two main types of phase-field evolution methods: one based on the Ginzburg-Landau model[17]; and the other based on the variational approach.[18] The latter is an extension of the classical Griffith's theory of fracture mechanics and has gradually become mainstream. While the phase-field method has a wide application in fracture problems, its inherent degradation functions and length scale parameter need to be further studied to better model the transition area of the cracked material.[19,20]

The eigenerosion method is a novel continuous method proposed by Pandolfi and Ortiz.[21] Similar to the phase-field model, this method is also formulated within a variational framework.[22] As a variant of the eigenfracture scheme,[23] the method approximates the crack-induced discontinuities by means of eigendeformations that enable the solids to develop displacement jumps that cost no local elastic energy. Specifically, the eigendeformations are restricted in a binary sense: they can be either 0, if the corresponding material neighborhood is failed, or 1, if the local material behavior is elastic. When combined with the finite element method (FEM), this scheme reduces to element erosion, which means that once the energy release rate accompanying the element exceeds the critical energy release rate G_c, the element will be eroded to describe the fracture. The eroded elements then lose load bearing capacity, and crack propagation continues. Hence, the propagation of the crack can establish a relationship with the various energy dissipation paths in materials. In addition, the eigenerosion approach has been proven to be comparable to other more complex numerical fracture schemes in terms of accuracy and convergence.[21,24-26] Furthermore, the solution of the method converges to those of Griffith-type fracture when the mesh size approaches to infinitesimal. All of these make the eigenerosion approach an attractive and promising method.

Despite the breadth of discretization approaches of governing equations, the aforementioned fracture models, continuous or discontinuous, are mainly paired with mesh-based methods because mesh-based methods are relatively developed and can easily handle boundary conditions. However, these mesh-based methods (eg, FEM) usually suffer from mesh distortion in the case of large deformation, thereby causing loss of accuracy. In addition, dealing with mesh distortion related issues is not a trivial task. Compared with the mesh-based methods, meshless approaches are generally free of a grid so that they can avoid mesh distortion problems. To date, several types of meshless approaches have been developed for fracture analysis; for instance, the element free Galerkin[27] method, smooth particle hydrodynamics,[28,29] peridynamics,[30,31] and the optimal transportation meshfree[22,24,25] method. These methods allow crack propagation in any direction and support arbitrarily large topological changes. The main difficulty is defining the "influence" zone of particles around the crack.[32] Fortunately, the material point method[33] (MPM) emerged as a feasible tool that can alleviate this issue. As a hybrid Eulerian-Lagrangian formulation, MPM discretizes a modeled object into a set of Lagrangian particles that move within a background grid. In MPM, computational information is transferred back and forth between material points (particles) and nodes of the background grid, which has the dual advantages of a meshless method and a mesh-based method.

MPM has been applied to study cracking problems because of its multiple merits. Nairn proposed an MPM-based fracture model termed CRAMP,[34] which performs two-dimensional (2D) crack simulation by tracking two velocity fields describing the motion "above" and "below" the crack plane. This allows crack paths to be explicitly captured. The 2D CRAMP was extended to 3D CRAMP[35,36] to simulate the dynamic three-dimensional (3D) crack propagation. Moreover, the decohesion model is also used to predict crack evolution.[37-39] Because the crack surface is implicitly described, this kind of method would fail to calculate the fracture parameters, which are

vital to the evaluation of crack propagation. More recently, Liang et al developed an MPM-based fracture simulation method by altering the shape function.[32] This method enriches the nodal degrees of freedom, just as the XFEM does. Another method worth mentioning is the phase-field MPM,[13,14] which combines a phase-field approach with MPM. As proved, this method can resolve intricate cracks; it, however, has limitations related to parameter tuning.[14]

Actually, almost all fracture models/methods used in a finite element framework can be applied to MPM. In this regard, we first introduce the eigenerosion approach into an MPM framework, aiming at developing an augmented MPM for the simulation of dynamic fracture in brittle materials. In the proposed method, the energy release rate of each particle controlling the crack propagation only needs to be calculated within its neighborhood domain. Moreover, the evaluation of a material's fracture behavior can be decoupled from the governing equations as a separate solution step. Therefore, the eigenerosion scheme can be easily integrated into any standard MPM solver with minor modifications. Furthermore, to distinguish the different effects of tension and compression on fracture behavior, we carry out a spectral decomposition method to decompose the elastic strain energy into tension and compression parts. Moreover, it is assumed that the tensile strain energy drives the crack evolution. Several benchmark tests for dynamic brittle fracture are presented to verify the proposed method.

This article is organized as follows. Section 2 gives a brief description of the variational theory of fracture, whereas Section 3 presents the standard MPM as well as the generalized interpolation material point (GIMP) scheme and the fracture model of eigenerosion. Next, the algorithmic implementation of the eigenerosion enhanced MPM is described in Section 4. Section 5 discusses the accuracy, efficiency, and robustness of the proposed method through several numerical examples. Some conclusions then are provided in Section 6.

2 | VARIATIONAL DESCRIPTION OF FRACTURE

In this section, we provide a brief variational description of brittle fracture in elastic solids, in accordance with References 12-14,18.

2.1 | Variational formulation

As a starting point, an arbitrary deformable body $\boldsymbol{\Omega} \subset \mathrm{R}^d$ ($d \in \{1, 2, 3\}$ is the dimension of the problem) with internal discontinuity boundary $\boldsymbol{\Gamma}$ and external boundary $\partial\boldsymbol{\Omega}$ is considered, as shown in Figure 1. The body is deformed under the action of applied loads including body forces, tractions, and prescribed displacements such that the initial domain $\boldsymbol{\Omega}_0$ in the reference configuration C_0 turns into $\boldsymbol{\Omega}_t$ in the current configuration C_t. The initial discontinuity $\boldsymbol{\Gamma}_0$ then evolves to $\boldsymbol{\Gamma}_t$, indicating crack propagation. The deformation map between the configurations is described by $\mathbf{x} = \varphi(\mathbf{X}, t)$, where $\mathbf{x}$ and $\mathbf{X}$ are spatial and material coordinates, respectively.

According to the variational theory of fracture, the total potential energy Ψ_{pot} of a perfectly brittle material is defined as

$$\Psi_{\mathrm{pot}} = \Psi_e + \Psi_f = \int_{\boldsymbol{\Omega}\backslash\boldsymbol{\Gamma}} \psi_e(\boldsymbol{\varepsilon})\mathrm{d}\boldsymbol{\Omega} + \int_{\boldsymbol{\Gamma}} \mathrm{G_c}\mathrm{d}\boldsymbol{\Gamma}, \tag{1}$$

where $\boldsymbol{\Omega}\backslash\boldsymbol{\Gamma}$ denotes the domain of the body with the crack set excluded, Ψ_e is the elastic potential energy, Ψ_f is the released energy at crack surfaces, ψ_e is the elastic strain energy density, $\boldsymbol{\varepsilon}$ is the strain tensor, and $\mathrm{G_c}$ is the critical energy release rate. In a quasistatic case, minimizing Ψ_{pot} leads to crack evolution,[14,40] with the idea being that fracture should occur in a way that corresponds to the minimal potential energy.

2.2 | Elasticity degradation

To account for the loss of bearing capacity of a solid body in the failure zone, the degradation effect of fracture is always exerted on the elastic energy. This is achieved by adopting a degradation function $g(c)$ superimposed on the elastic strain
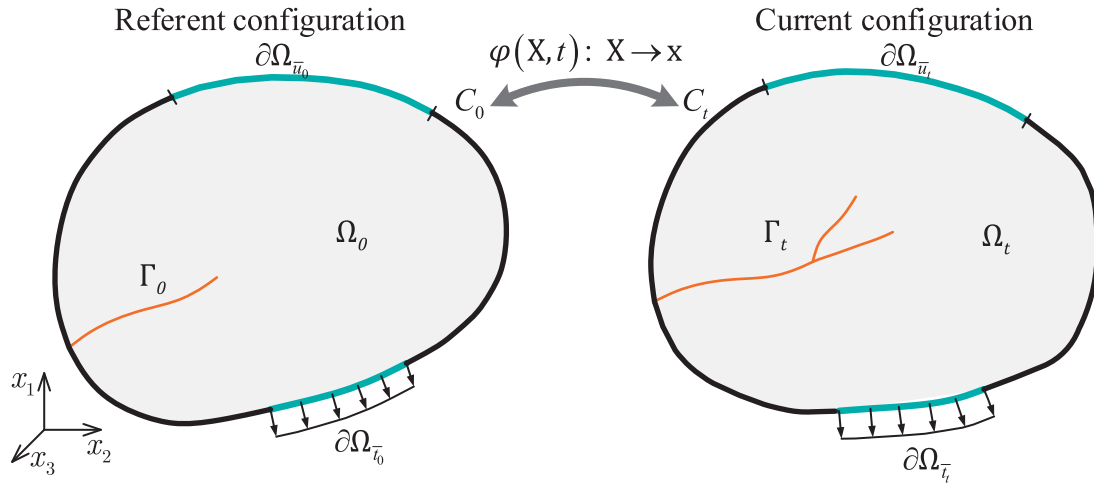
Referent configuration $\partial\Omega_{\overline{u}_0}$ C_0

$\varphi(\mathrm{X},t): \mathrm{X}\rightarrow\mathrm{x}$

Current configuration $\partial\Omega_{\overline{u}_t}$ C_t

Ω_0

Γ_0

x_1
x_3 x_2

$\partial\Omega_{\overline{t}_0}$

Γ_t

Ω_t

$\partial\Omega_{\overline{t}_t}$

FIGURE 1 Schematic representation of a solid body $\boldsymbol{\Omega}$ with discontinuity boundary $\boldsymbol{\Gamma}$ in the reference and current configuration [Color figure can be viewed at wileyonlinelibrary.com]

energy density. Furthermore, to enforce the crack propagation only in tension, the elastic energy is additively decomposed into positive and negative parts. ψ_e is then rewritten as

$$\psi_e(\boldsymbol{\varepsilon}, c) = g(c)\psi_e^+(\boldsymbol{\varepsilon}) + \psi_e^-(\boldsymbol{\varepsilon}), \tag{2}$$

where c is the damage field, and ψ_e^+ and ψ_e^- are the strain energy densities computed from the positive and negative components of the strain tensor, respectively. Specifically,

$$\psi_e^+(\boldsymbol{\varepsilon}) = \frac{\lambda}{2}\langle\mathrm{tr}[\boldsymbol{\varepsilon}]\rangle_+^2 + \mu\mathrm{tr}[(\boldsymbol{\varepsilon}_+)^2] \tag{3}$$

$$\psi_e^-(\boldsymbol{\varepsilon}) = \frac{\lambda}{2}\langle\mathrm{tr}[\boldsymbol{\varepsilon}]\rangle_-^2 + \mu\mathrm{tr}[(\boldsymbol{\varepsilon}_-)^2] \tag{4}$$

with the two bracket operators being $\langle x\rangle_+ = (x+|x|)/2$, $\langle x\rangle_- = (x-|x|)/2$, and λ and μ being the Lamé constants. The positive and negative strain tensors are given by

$$\boldsymbol{\varepsilon}_+ = \sum_{i=1}^{d}\langle\varepsilon_i\rangle_+\mathbf{n}_i\otimes\mathbf{n}_i, \tag{5}$$

$$\boldsymbol{\varepsilon}_- = \boldsymbol{\varepsilon} - \boldsymbol{\varepsilon}_+, \tag{6}$$

where $\{\varepsilon_i\}_{i=1\ldots d}$ are the principal strains and $\mathbf{n}$ consists of the orthonormal eigenvectors of $\boldsymbol{\varepsilon}$.

The Cauchy elastic stress tensor is readily defined by

$$\boldsymbol{\sigma} = g\frac{\partial\psi_e^+}{\partial\boldsymbol{\varepsilon}} + \frac{\partial\psi_e^-}{\partial\boldsymbol{\varepsilon}} = g\boldsymbol{\sigma}_+ + \boldsymbol{\sigma}_-, \tag{7}$$

where $\boldsymbol{\sigma}_+ = \lambda\langle\mathrm{tr}[\boldsymbol{\varepsilon}]\rangle_+\mathbf{I} + 2\mu\boldsymbol{\varepsilon}_+$ and $\boldsymbol{\sigma}_- = \lambda\langle\mathrm{tr}[\boldsymbol{\varepsilon}]\rangle_-\mathbf{I} + 2\mu\boldsymbol{\varepsilon}_-$ are the tensile and compressive stress tensor, respectively.

3 | MPM FOR BRITTLE FRACTURE

In the updated Lagrangian formulation, the weak form of governing equations including the momentum equation and the traction boundary equation is given by References 32,41

$$\int_{\boldsymbol{\Omega}}\rho a_i\delta u_i d\boldsymbol{\Omega} + \int_{\boldsymbol{\Omega}}\sigma_{ij}\delta u_{i,j}d\boldsymbol{\Omega} - \int_{\boldsymbol{\Omega}}\rho b_i\delta u_i d\boldsymbol{\Omega} - \int_{\Gamma_s}\overline{t}_i\delta u_i d\boldsymbol{\Gamma} = 0, \tag{8}$$

where ρ is the current material density, $\boldsymbol{\Gamma}_s$ denotes the traction boundary of material domain $\boldsymbol{\Omega}$, b is the body force, $\bar{t}$ is the traction, u is the displacement, and a is the acceleration.

3.1 | MPM spatial discretization

MPM is a hybrid Eulerian-Lagrangian discretization scheme for solid mechanics. In MPM, the continuum solid body is discretized into a set of particles. Each particle is assigned the information of position, mass, velocity, volume, strain, and stress, which are denoted by $\mathbf{x}_p$, m_p, $\mathbf{v}_p$, V_p, $\boldsymbol{\varepsilon}_p$, and $\boldsymbol{\sigma}_p$, respectively, as well as all other relevant variables necessary for the specific material model. The Eulerian background grid serves as a computational scratch pad for the momentum solution. Hence, the particle displacement, u_{ip}, can be obtained through the following equation:

$$u_{ip} = \sum_{I=1}^{n_g} N_{Ip} u_{iI},$$ (9)

where the subscript i denotes the components of a spatial variable, the subscript I indicates the node index, the subscript p indicates the particle index, n_g is the number of background grid nodes influencing the particle p, and N_{Ip} is the shape function of the background grid cell. In a standard MPM, the linear shape function is always used for its simplicity.

Because the continuum bodies are discretized into particles, the density of bodies can be given by

$$\rho(\mathbf{x}) = \sum_{p=1}^{n_p} m_p \delta(\mathbf{x} - \mathbf{x}_p),$$ (10)

where n_p denotes the total number of particles, and δ is the Dirac delta function. Furthermore, by treating the particles as the integral points in the weak form of Equation (8), it can be deduced that

$$m_I a_{iI} = f_{iI}^{\text{int}} + f_{iI}^{\text{ext}},$$ (11)

where m_I is the lumped mass of grid node I, represented by

$$m_I = \sum_{p=1}^{n_p} N_{Ip} m_p$$ (12)

f_{iI}^{int} and f_{iI}^{ext} are the internal nodal force and external nodal force, which are separately given as

$$f_{iI}^{\text{int}} = -\sum_{p=1}^{n_p} \frac{m_p}{\rho_p} N_{Ip,j} \sigma_{ijp},$$ (13)

$$f_{iI}^{\text{ext}} = \sum_{p=1}^{n_p} m_p N_{Ip} b_{ip},$$ (14)

where $N_{Ip,j}$ is the gradient of the shape function N_{Ip} in the j-direction. When a linear shape function is adopted, the value of $N_{Ip,j}$ jumps at cell interfaces, resulting in numerical noise. Two issues are associated with the numerical noise. First, huge forces would occur on a node with tiny mass, leading to numerical oscillation. Second, the gradient discontinuity causes discontinuity of the force. The above problems would render unphysical results when large deformation happens.

3.2 | Generalized interpolation material point

The GIMP method proposed by Bardenhagen and Kober[42] is a generalized form of the traditional MPM that allows a C^1 order of shape function between particles and grid nodes to mitigate the cell crossing noise. Currently, there are
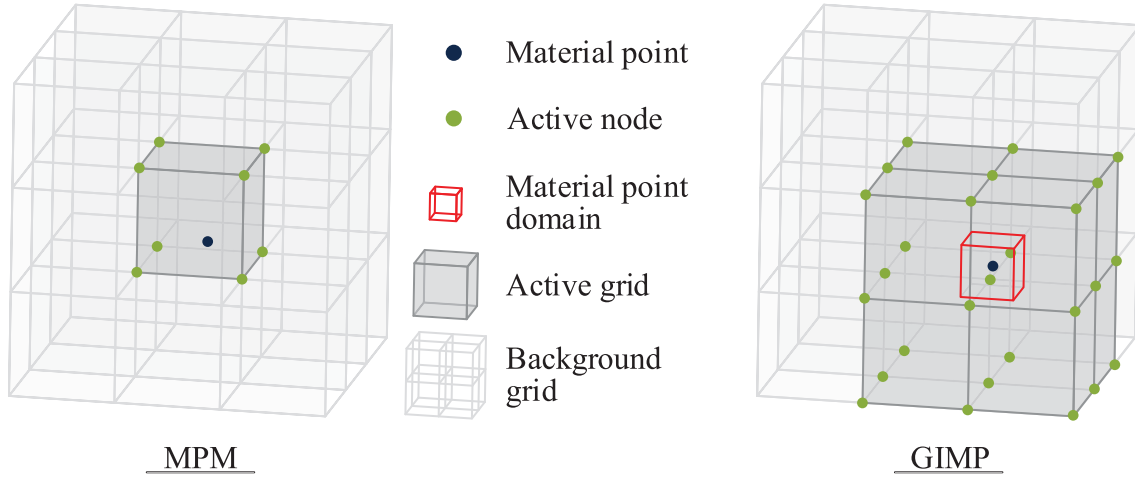
FIGURE 2 Schematic of different mapping schemes in MPM and GIMP. GIMP, generalized interpolation material point; MPM, material point method [Color figure can be viewed at wileyonlinelibrary.com]

several types of GIMP methods, for instance, the contiguous particle GIMP where particles are assumed contiguous, and the undeformed GIMP[43] (uGIMP) where particles are assigned fixed size. In this study, uGIMP is used. For uGIMP, the following smoothed shape functions are employed

$$N_{Ip} = s(\xi_x)s(\xi_y)s(\xi_z) \tag{15}$$

for 3D problems, where $\xi_x = |x_p - x_i|/L$, $\xi_y = |y_p - y_i|/L$, and $\xi_z = |z_p - z_i|/L$, L is the cell length. Interpolation function $s(\xi)$ is given by

$$s(\xi) = \begin{cases} \frac{7-16\xi^2}{8}, & \xi \leq 0.25 \\ 1 - \xi, & 0.25 < \xi \leq 0.75 \\ \frac{(5-4\xi)^2}{16}, & 0.75 < \xi \leq 1.25 \\ 0, & \xi > 1.25 \end{cases}. \tag{16}$$

The GIMP shape function is inherently smooth with a larger support area (see the right in Figure 2) and has continuous gradients.

3.3 | Fracture model

3.3.1 | Preexisting crack treatment

Although not suffering from mesh distortion, traditional MPM automatically maintains a single velocity field, which makes it difficult to model the sharp separation of materials.[44] Therefore, an additional approach of describing the discontinuity is required to realize a physical discontinuity on both sides of the crack surface. In this article, we propose a novel phantom-node method to handle the cracks initially existing in the solid body. This method does not require the establishment of multiple velocity fields. Instead, only phantom nodes need to be added near the preexisting crack (see Figure 3). The spatial coordinates of phantom nodes are the same as those of the original nodes being replaced, ensuring that the position judgment of particles (ie, the determination of which grid these particles are in) and the mapping process are not affected. It should be noted that for a clear illustration of Figure 3, the locations of the phantom nodes are displayed to be different from those of the replaced nodes. Compared with the original procedure, the proposed method only introduces a small number of grid nodes, which adds little overhead to the existing computations.
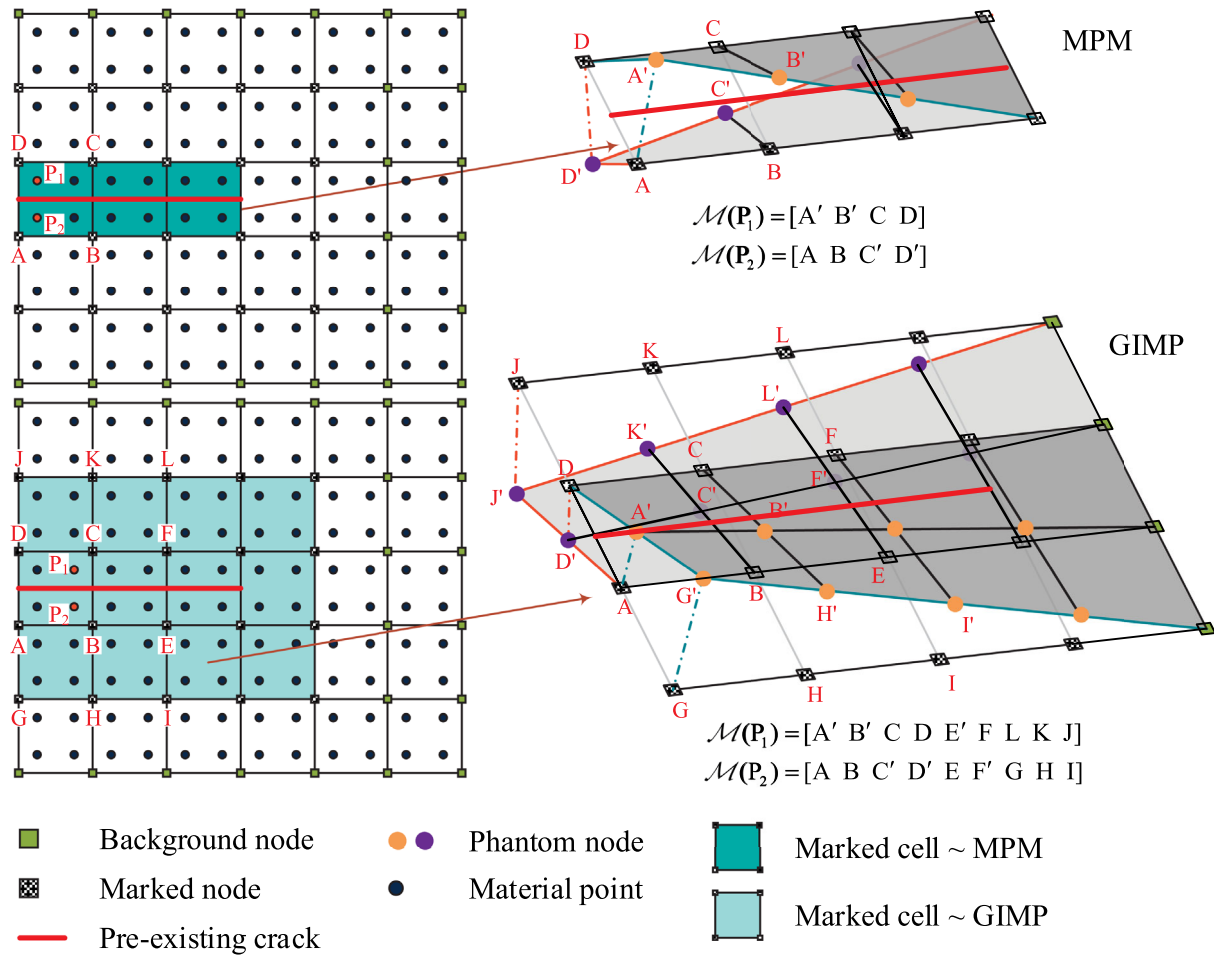
FIGURE 3 Schematic illustration of the preexisting crack treatment using phantom nodes in MPM and GIMP. GIMP, generalized interpolation material point; MPM, material point method [Color figure can be viewed at wileyonlinelibrary.com]

In the phantom-node method, the replaced node is called the marked node, and similarly, the cell surrounded by the replaced node is called the marked cell. Taking 2D as an example, the marked cells in MPM correspond to the cells where the preexisting crack is located (see the dark cyan zone in Figure 3), while in GIMP the adjacent cells (see the light cyan zone in Figure 3) are also included because GIMP has a larger support area for its shape function. When a particle moves into a marked cell, the treatment for this particle relies on its position relative to the preexisting crack. Here, we let $\mathcal{M}(P)$ be the mapping nodes set for the particle P. In Figure 3, particles P_1 and P_2 are in different positions relative to the preexisting crack. Then, the mapping node sets are $\mathcal{M}(P_1) = [A' \ B' \ C \ D]$ and $\mathcal{M}(P_2) = [A \ B \ C' \ D']$ for MPM, whereas those for GIMP are $\mathcal{M}(P_1) = [A' \ B' \ C \ D \ E' \ F \ L \ K \ J]$ and $\mathcal{M}(P_2) = [A \ B \ C' \ D' \ E \ F' \ G \ H \ I]$. The numbered nodes with superscript (eg, A' and B') represent the phantom nodes, while the ones without superscript (eg, A and B) represent the marked nodes. The superscripted nodes have the same spatial coordinates as their corresponding nonsuperscripted nodes; for instance, the coordinates of A' and A are the same. It should be noted that Figure 3 shows only the horizontal crack in the case of 2D. It is, however, not difficult to extend this method to the more general case of 3D inclined cracks, provided the particles are refined in the vicinity of the crack.

3.3.2 | Eigenerosion approach

Within the context of the MPM formulation, fracture can be simulated by failing particles according to an energy release criterion. When the particles fail, they are excluded from the computation of the stresses filed, which characterizes the
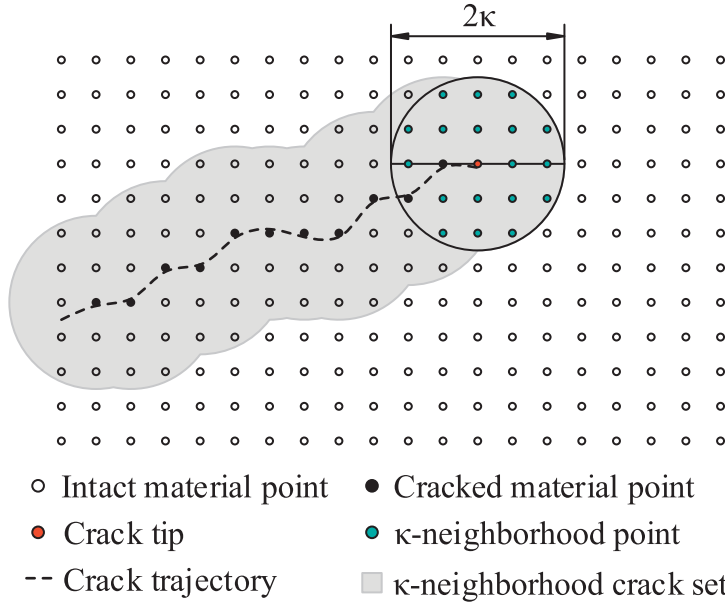
FIGURE 4 Visualization of the κ-neighborhood (shadowed area) of the crack set A [Color figure can be viewed at wileyonlinelibrary.com]

○ Intact material point ● Cracked material point
● Crack tip ● κ-neighborhood point
-- Crack trajectory ▨ κ-neighborhood crack set

evolution of cracks. This is termed as the eigenerosion algorithm by Pandolfi and Ortiz.[21] The algorithm tracks the mechanical degradation of material via a binary scalar damage variable (c), which, in general, equals "0" for a damaged material or "1" for an intact material. Following the References 21-24,26, the fracture energy Ψ_f in Equation (1) can be rewritten as

$$\Psi_f = \mathsf{G_c}|A|, \tag{17}$$

where $|A|$ denotes the area of the crack set. Because a mathematical description of the crack set A is difficult to derive in engineering applications, the eigendeformation field ε^* is introduced in the eigenerosion approach as an alternative to numerically approximate the problem. Instead of producing the exact crack surfaces, the eigenerosion approach seeks to approximate the fracture within the κ-neighborhood (κ is a parameter with units of length). Therefore, the crack-tracking problem in elastic brittle materials can be simplified as the variation of

$$L(\mathbf{u}, \varepsilon^*) = \int_{\Omega \backslash A} \{g(c)\psi_e^+(\varepsilon) + \psi_e^-(\varepsilon)\}d\Omega + \mathsf{G_c}\frac{|C_\kappa|}{2\kappa} - \int_{\Omega \backslash A} \frac{1}{2}\rho \mathbf{v} \cdot \mathbf{v}d\Omega, \tag{18}$$

where C_κ is the κ-neighborhood support of the eigendeformation field (an approximation of crack surface by volume domain of κ-neighborhood), and $|C_\kappa|$ denotes the volume of C_κ, as shown in Figure 4.

To describe the influence of fracture on the material, the degradation function is assumed to be $g(c) = c$ in this study. In addition, only the positive part of the elastic strain energy ψ_e^+ is assumed to drive the crack propagation. Thus, within the framework of eigenerosion theory,[21,22,24,25,45] the effective energy release rate $\mathsf{G_p}$ of particle p can be given by

$$\mathsf{G_p} = \frac{\alpha\kappa}{\overline{m}_p} \sum_{\mathbf{x}_q \in C_\kappa^p} m_q \psi_e^+(\varepsilon) \tag{19}$$

with

$$\overline{m}_p = \sum_{\mathbf{x}_q \in C_\kappa^p} m_q, \tag{20}$$

where C_κ^p is the κ-neighborhood of particle p, denoting the ball of radius κ centered at $\mathbf{x}_p$ for 3D, or the circle of radius κ centered at $\mathbf{x}_p$ for 2D; α is the normalizing constant ranging from 1 to 2^{24}; and $\overline{m}_p$ is the mass of the κ-neighborhood. The calculation of $\mathsf{G_p}$ needs to search for κ-neighborhood particles, which can be realized using the cell-linked method suggested by Allen and Tildesley.[46] Note that the eroded (ie, whose $\mathsf{G_p}$ exceeds $\mathsf{G_c}$) particles are excluded from the calculation of effective energy release rate.

FIGURE 5 Algorithm flow of the eigenerosion enhanced MPM/GIMP. GIMP, generalized interpolation material point; MPM, material point method [Color figure can be viewed at wileyonlinelibrary.com]
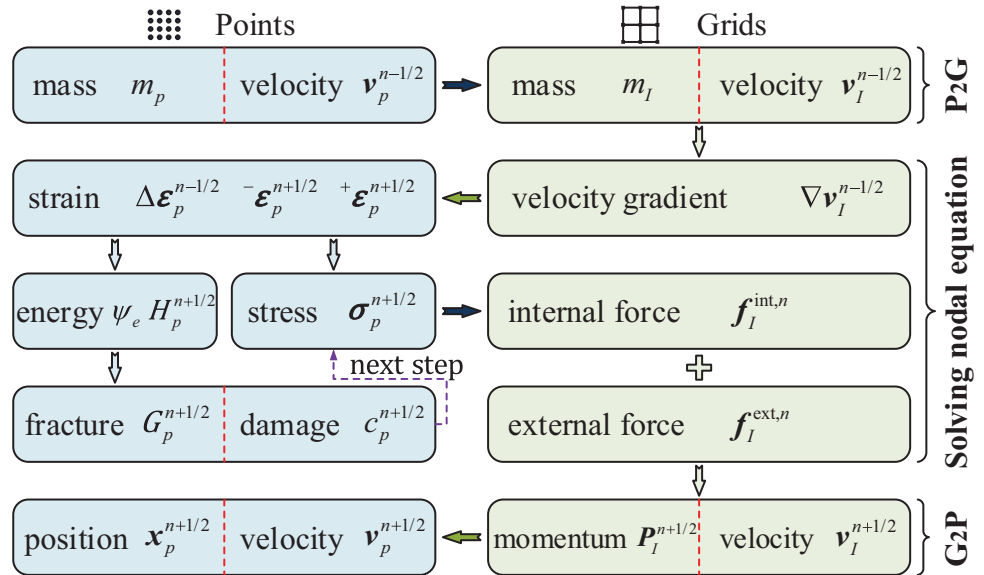
Because of the irreversibility of fracture, the crack set A should obey the constraint: $A(t) \subseteq A(t + dt)$. This can be realized by introducing a strain-history field, H, which satisfies the Kuhn-Tucker conditions for loading and unloading.

$$\text{H} \geq \psi_e^+, \dot{H} \geq 0, \dot{H}(\psi_e^+ - \text{H}) = 0. \tag{21}$$

Alternatively,

$$\text{H}(\mathbf{x}, t) = \max_{s \in [0,t]} \psi_e^+ [\boldsymbol{\varepsilon}(\mathbf{x}, s)]. \tag{22}$$

After substituting H for ψ_e^+ in Equation (19), we obtain the modified equation for G_p

$$\text{G}_\text{p} = \frac{\alpha \kappa}{m_p} \sum_{\mathbf{x}_q \in C_\kappa^p} m_q \text{H}. \tag{23}$$

The material point is failed if

$$\text{G}_\text{p} \geq \text{G}_\text{c}. \tag{24}$$

For linear elasticity, the criteria of Equations (23) and (24) have been proved to lead to an approximation that converges to the Griffith fracture in the limit of vanishingly small discretization according to Γ-convergence theorems.[23,25,45] In addition, the averaging of energy over an intermediate κ-neighborhood for the calculation of G_p has the advantage of eliminating spurious mesh-dependent artifacts.[22]

4 | ALGORITHMIC IMPLEMENTATION

4.1 | Eigenerosion enhanced MPM/GIMP solution scheme

Explicit schemes are usually used in MPM/GIMP because they require less computational memory and are easier to implement than implicit schemes. This study employs the central difference method together with the update-stress-first scheme[47] to solve the governing equations. The algorithmic implementation of the eigenerosion enhanced MPM/GIMP (EigenMPM) involves the following steps (see Figure 5):

(1) **Initialization**. Each particle is initialized to have a mass m_p, volume V_p^0, initial position $\mathbf{x}_p^0$, initial velocity $\mathbf{v}_p^0$, and material-related parameters (such as the Lamé constants in the case of elasticity).

(2) **Mapping from particle to grid (P2G)**. At the start of every time step n, particle mass and momentum are transferred to the background grid nodes, namely, Equation (12) and

$$\mathbf{P}_I^{n-1/2} = \sum_{p=1}^{n_p} m_p v_p^{n-1/2} N_{Ip}^n. \tag{25}$$

(3) **Boundary condition imposition**. The prescribed essential boundary conditions are imposed on the grid node. At the fixed boundary, set $P_{iI}^{n-1/2} = 0$.

(4) **Grid nodal velocity computation**. The grid nodal velocity can be calculated with

$$\mathbf{v}_I^{n-1/2} = \frac{\mathbf{P}_I^{n-1/2}}{m_I^n}. \tag{26}$$

(5) **Eigenerosion computation**.

(i) *Particle strain evolution*. The particle strain increment is calculated using the node velocity gradient, which reads

$$\Delta \varepsilon_p^{n-1/2} = \Delta t \sum_{I=1}^{n_g} \frac{1}{2} \left(\nabla N_{Ip} \mathbf{v}_I^{n-1/2} + \left(\nabla N_{Ip} \mathbf{v}_I^{n-1/2} \right)^T \right). \tag{27}$$

Then, the particle strain is updated by $\varepsilon_p^{n+1/2} = \varepsilon_p^{n-1/2} + \Delta \varepsilon_p^{n-1/2}$. After the spectral decomposition by Equations (5) and (6), $\varepsilon_p^{n+1/2}$ is decomposed into $^-\varepsilon_p^{n+1/2}$ and $^+\varepsilon_p^{n+1/2}$.

(ii) *Particle stress evolution*. The particle stress $\boldsymbol{\sigma}_p^{n+1/2}$ is calculated using Equation (7).

(iii) *Particle energy evolution*. The particle energy related parameters ψ_e^+ and $\mathtt{H}$ are calculated using Equations (3) and (22).

(iv) *Eigenerosion computation*. The effective energy release rate $\mathtt{G}_p^{n+1/2}$ is calculated using Equation (23). If $\mathtt{G}_p^{n+1/2}$ surpasses $\mathtt{G}_c$, the damage field is $c_p^{n+1/2} = 0$, indicating that particle p is eroded and the crack propagates. Otherwise, $c_p^{n+1/2} = 1$.

(6) **Explicit force computation**. The grid nodal internal force $\mathbf{f}_I^{\mathrm{int},n}$ is obtained using Equation (13) while the external force $\mathbf{f}_I^{\mathrm{ext},n}$ is given by adding the contribution of traction $\bar{\mathbf{t}}$ based on Equation (14); then,

$$\mathbf{f}_I^{\mathrm{ext},n} = \sum_{p=1}^{n_p} m_p N_{Ip}^n \mathbf{b}_p^n + \sum_{p=1}^{n_p} N_{Ip}^n \bar{\mathbf{t}}_p^n h^{-1} \frac{m_p}{\rho_p}. \tag{28}$$

The total nodal force $\mathbf{f}_I^n$ is calculated by $\mathbf{f}_I^n = \mathbf{f}_I^{\mathrm{int},n} + \mathbf{f}_I^{\mathrm{ext},n}$. For the fixed boundary, set $f_{iI}^n = 0$.

(7) **Grid nodal momentum update**. The grid nodal momentum is updated by

$$\mathbf{P}_I^{n+1/2} = \mathbf{P}_I^{n-1/2} + f_I^n \Delta t^n \tag{29}$$

(8) **Mapping from grid to particle (G2P)**. The particle velocity and position are updated from the grid with

$$\mathbf{v}_p^{n+1/2} = \mathbf{v}_p^{n-1/2} + \Delta t^n \sum_{I=1}^{n_g} \frac{\mathbf{f}_I^n N_{Ip}^n}{m_I^n}, \tag{30}$$

$$\mathbf{x}_p^{n+1} = \mathbf{x}_p^n + \Delta t^{n+1/2} \sum_{I=1}^{n_g} \frac{\mathbf{P}_I^{n+1/2} N_{Ip}^n}{m_I^n}. \tag{31}$$

(9) **Cell lists reconstruction**. Because particles move to new positions, cell lists should be reconstructed for the next time step of κ-neighborhood particle search. A detailed description will be provided in the following section.

It is clear that for a standard MPM/GIMP elasticity framework with explicit integration, only three additional steps (strain decomposition, eigenerosion computation, and cell lists construction) are needed for brittle fracture simulation.
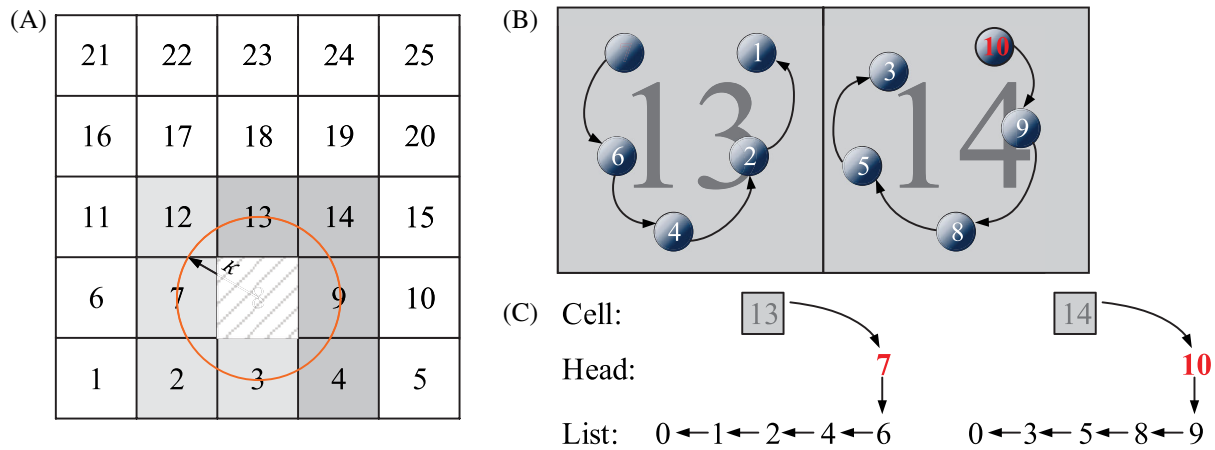
FIGURE 6 Cell-linked method in two dimensions. (A) Schematic diagram of auxiliary cells with size equal to κ; (B) A close-up of cells 13 and 14, indicating the particles and the link-list structure; (C) The `head` and `list` array elements corresponding to the two cells 13 and 14 [Color figure can be viewed at wileyonlinelibrary.com]

4.2 | Cell-linked method for κ-neighborhood particle search

In the EigenMPM, the κ-neighborhood particle search for the calculation of effective energy release rate is performed by a cell-linked method, as suggested by Allen and Tildesley.[46] In the cell-linked method, as shown in Figure 6, auxiliary cells with size equal to κ are created. At the beginning of fracture calculation, the connection between cells needs to be established. For the 2D system illustrated, each cell only needs to correlate with the cells in its upper right direction (eg, cells 4, 9, 13, 14 for cell 8). The connection of cells would not change once it is established. At every time step, each cell needs to update the memorization of its belonging particles (ie, cell lists construction), and this is achieved by renewing two arrays—the "head-of-chain" array (`head`) and the linked-list array (`list`). Specifically, the `head` array stores the particles with the largest number in each cell, while the `list` array stores the numbering order of the particles in each cell (see Figure 6B,C). Therefore, the κ-neighborhood particles can be efficiently found.

5 | NUMERICAL EXAMPLES

The proposed EigenMPM has been implemented in the Fortran code for general 3D boundary value problems. To validate the proposed method, the following numerical experiments are considered: the L-shaped panel test, the dynamic crack branching of a plate, the edge-cracked plate under impulsive loading, and the John-Shah test. Except for the first experiment, the other three all have preexisting cracks. The preexisting crack is modeled by the phantom-node algorithm described in Section 3.3.1, and the propagating crack is represented by the eigenerosion damage field evolution. It should be noted that the initial crack can also be approximated by setting dense eroded particles close to the actual crack boundary. However, such an approach is not accurate enough because it is a result of a smeared approximation. In all tests, external loads, including body forces and tractions, are directly applied at material points, which is in line with those reported in Reference 13. In addition, kinematic boundaries, such as velocity boundaries, are dynamically imposed on the background grid by monitoring the positions of boundary particles.

Results obtained from the EigenMPM are compared with those of other methods from the literature in terms of the crack path and other pertinent quantities. Simulation parameters, that is, normalizing constant α and neighborhood size κ, will also be discussed.

5.1 | L-shaped panel test

To gain a first insight into the performance of the brittle fracture model proposed herein, we consider a well-studied L-shaped panel test, which was first reported by Winkler.[48] The geometry, boundary conditions of the specimen, as well
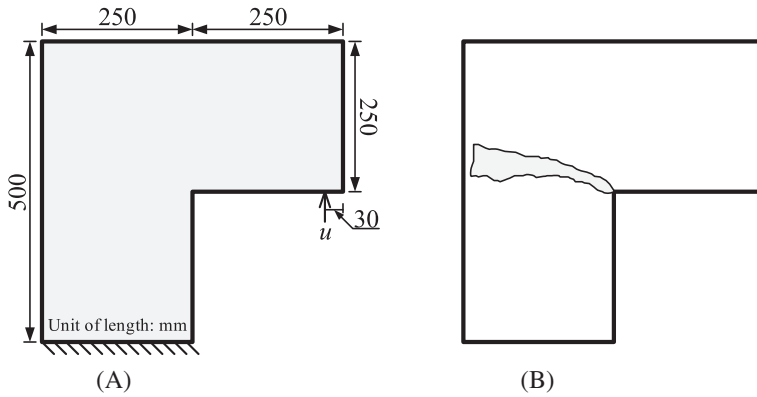
FIGURE 7 L-shaped panel test. (A) Geometry and boundary conditions; (B) experimentally observed crack pattern envelope[48]

TABLE 1 Influence of simulation parameters in L-shaped panel test

Background grid size $h = 5\,\text{mm}$					
	Critical vertical displacement (mm)			**Critical load (kN)**		
	κ			κ		
α	**0.9**	**1.1**	**1.25**	**0.9**	**1.1**	**1.25**
1.0	0.284	0.284	0.291	17.300	17.230	17.577
1.5	0.245	0.245	0.251	15.100	15.082	15.394
2.0	0.222	0.222	0.223	13.737	13.758	14.046

as the resulting envelope of crack propagation paths are depicted in Figure 7. The specimen is constrained at the bottom edge. A vertical displacement loading is applied 30 mm from the right edge. The material properties are chosen as follows: Young's modulus $E = 25.85$ GPa, Poisson's ratio $\upsilon = 0.18$, energy release rate $G_c = 89$ N/m, tensile strength $\sigma_c = 2.7$ MPa, and mass density $\rho = 2500$ kg/m^3.

To investigate the influence of simulation parameters, we consider nine different combinations of normalizing constant α and neighborhood size κ, namely, the nine orthogonal combinations of $\alpha = \{1.0, 1.5, 2.0\}$ and $\kappa = \{0.9, 1.1, 1.25\,h\}$. Here, h indicates the background grid size. These nine simulations are performed under displacement control with a constant velocity of 0.01 m/s. The computational domain is discretized into 30 000 uniformly distributed material particles with the background grid size $h = 5$ mm. The derived results are shown in Table 1 where it can be seen that for the same neighborhood size, the normalizing constant α influences both the critical load and the critical vertical displacement. Figure 8 shows the crack paths. Here, the blue and red colors indicate intact and damaged material, respectively. As can be seen from Figure 8, the normalizing constant α has little effect on the final crack morphology. Considering that α appears in the numerator of the Equation (19) as a regulator, it mainly controls the initiation speed of cracks. Conversely, the neighborhood size κ affects the crack pattern a lot. This is reflected in two aspects: (i) a larger value of κ leads to a thicker failure zone; (ii) a smaller κ tends to produce flatter cracks.

The load-displacement curves are summarized in Figure 9, which shows that for the same normalizing constant, the impact of the neighborhood size κ on both the maximum reaction force and the critical vertical displacement is marginal. In other words, κ hardly affects crack initiation. However, when cracks occur, the reaction force drops faster with decreasing value of κ. This shows that the smaller the value of κ for a given grid size, the more obvious the local erosion effect due to the eigenerosion evolution. In particular, when the κ-neighborhood is reduced to cover only the particles themselves, the eigenerosion approach is generalized to a single particle erosion form. The single particle erosion is problematic and may suffer from spurious mesh-dependent artifacts.[22,25] Although $\kappa = 0.9\,h$ is also selected from the suggested range (see Equation (A3)), all the simulations with $\kappa = 0.9\,h$ fail to get good results (see Figure 8A,D,G). However, the simulations with $\kappa = 1.1\,h$ and $\kappa = 1.25\,h$ are capable of producing crack patterns that match well with the experimental observation. Hence, to avoid obvious effects of local erosion, the value of κ should not be too small.

To further investigate the effect of spatial discretization size, three cases are examined for the background grid size h, namely, $h = 10$, $h = 5$, and $h = 2.5$ mm. The corresponding number of particles for each case are 7500, 30 000, and
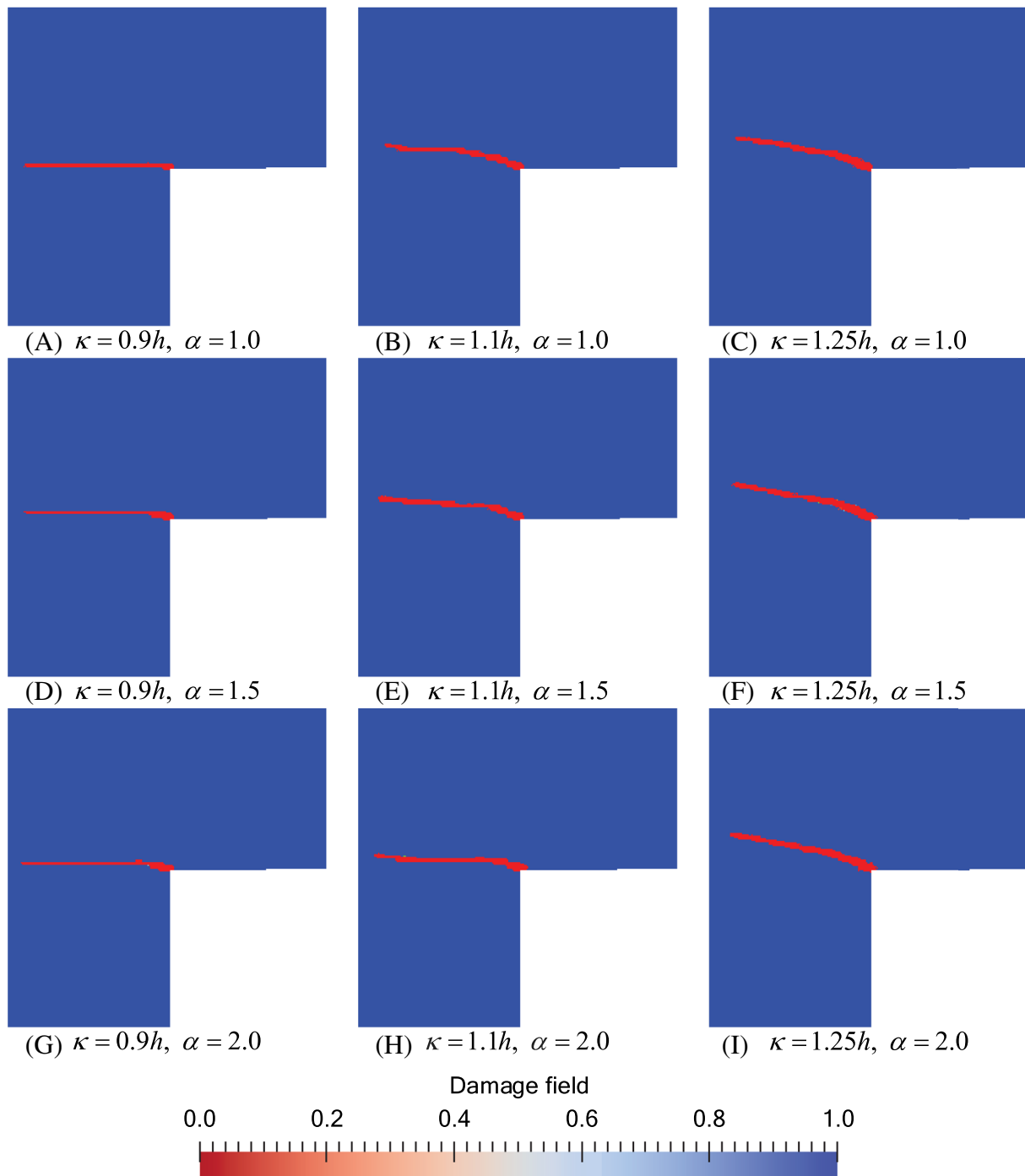
FIGURE 8 L-shaped panel test. Numerical crack patterns for various combinations of parameters κ and α [Color figure can be viewed at wileyonlinelibrary.com]

120 000, respectively. Meanwhile, three cases are considered for the neighborhood size κ, namely, $\kappa=$ {0.9, 1.1, 1.25 h} while the normalizing constant α is kept constant as 1.5. The obtained crack paths are shown in Figure 10, while the load-displacement curves are shown in Figure 11. As can be seen, the crack paths obtained from both grid sizes are almost the same. The only difference is that the fine discretization model results in a narrower crack trajectory. In addition, for the same neighborhood size κ, the load-displacement curves obtained by the three discretization models differ slightly. Critical values of reaction forces and vertical displacement are shown in Table 2 where it can be seen that the critical reaction force slightly decreases with decreasing grid density: this is in accordance with the results presented by Kakouris and Triantafyllou.[13]
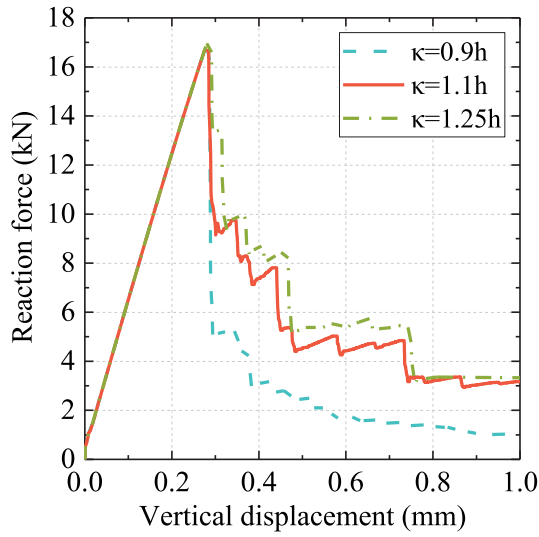
(A) $\alpha = 1.0$
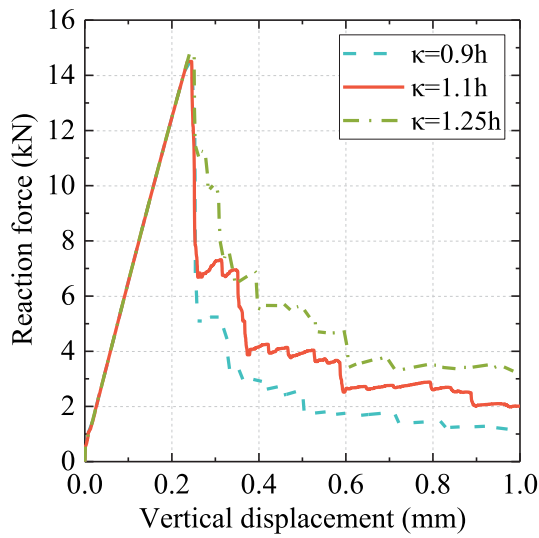
(B) $\alpha = 1.5$
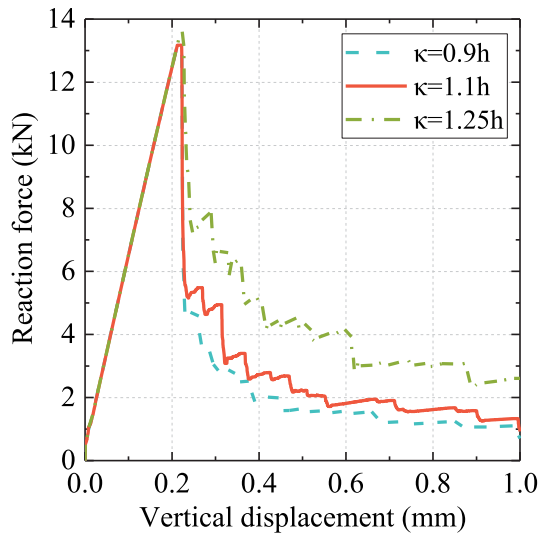
(C) $\alpha = 2.0$

FIGURE 9 Load-displacement curves for L-shaped panel test at different values of α [Color figure can be viewed at wileyonlinelibrary.com]

(A) $h = 10.0$ mm , $\kappa = 0.9h$ (B) $h = 10.0$ mm , $\kappa = 1.1h$ (C) $h = 10.0$ mm , $\kappa = 1.25h$

(D) $h = 5.0$ mm , $\kappa = 0.9h$ (E) $h = 5.0$ mm , $\kappa = 1.1h$ (F) $h = 5.0$ mm , $\kappa = 1.25h$

(G) $h = 2.5$ mm , $\kappa = 0.9h$ (H) $h = 2.5$ mm , $\kappa = 1.1h$ (I) $h = 2.5$ mm , $\kappa = 1.25h$

Damage field

0.0   0.2   0.4   0.6   0.8   1.0

Figure 12 shows the simulated crack paths for the case of $h = 5$ mm and $\kappa = 1.1 h$, and the case of $h = 2.5$ mm and $\kappa = 1.1 h$. Good agreement is achieved between the simulations and the experiment in terms of the crack path. Figure 13 compares different numerical and experimental curves of load-displacement. As observed, the result obtained by the EigenMPM is comparable to results of other methods from the literature.[13,49] It should be noted, however, that the numerical methods listed here both give a higher peak load than the experimental result. This is mainly because the critical strength condition of the material is not fully satisfied in these simulations. During the simulation of brittle fracture, the crack nucleation stress is likely to exceed the tensile strength of the material, which is allowed in a Griffith-type fracture theory.[12] After the crack nucleation, the structural responses of the material obtained by these numerical models (see Figure 13) are close to the experimental result.

5.2 | Dynamic crack branching

The second benchmark concerns a precracked rectangular plate and is used to evaluate the performance of the proposed model in solving problems involving crack branching. The geometry and loading boundary conditions of the plate are depicted in Figure 14. This problem has been extensively studied using different methods, such as, the XFEM,[50,51] phase-field method,[12,52] and peridynamics.[30,53] However, the material and boundary conditions used in
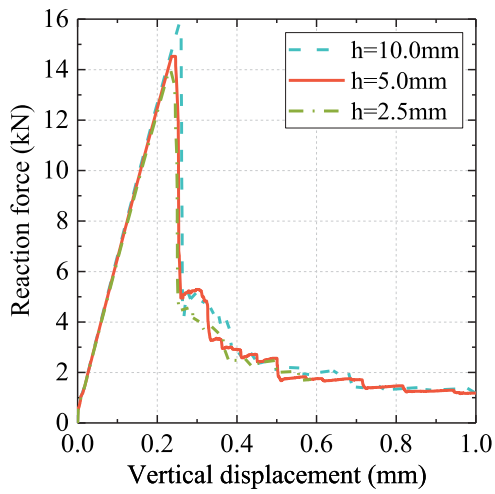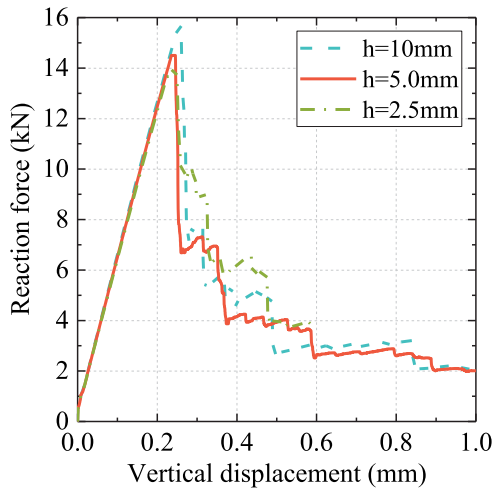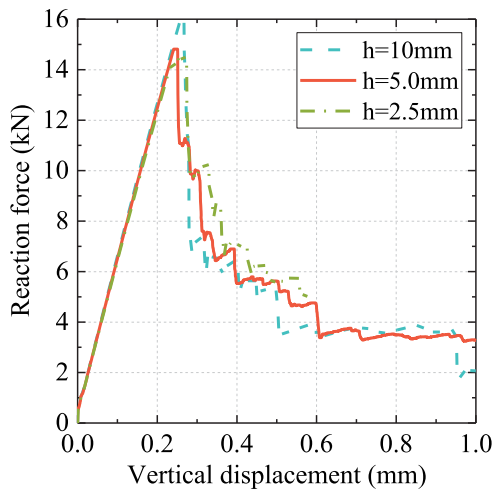
(A) $\kappa = 0.9h$

(B) $\kappa = 1.1h$

(C) $\kappa = 1.25h$

FIGURE 11 Load-displacement curves for L-shaped panel test at different values of κ [Color figure can be viewed at wileyonlinelibrary.com]

TABLE 2 Influence of spatial discretization size in L-shaped panel test

Simulation parameter $\alpha = 1.5$						
	Critical vertical displacement (mm)			Critical load (kN)		
	κ			κ		
Grid size (mm)h	0.9	1.1	1.25	0.9	1.1	1.25
10.0	0.259	0.260	0.267	16.101	16.143	16.532
5.0	0.245	0.245	0.251	15.100	15.082	15.394
2.5	0.243	0.249	0.253	14.463	14.499	14.710
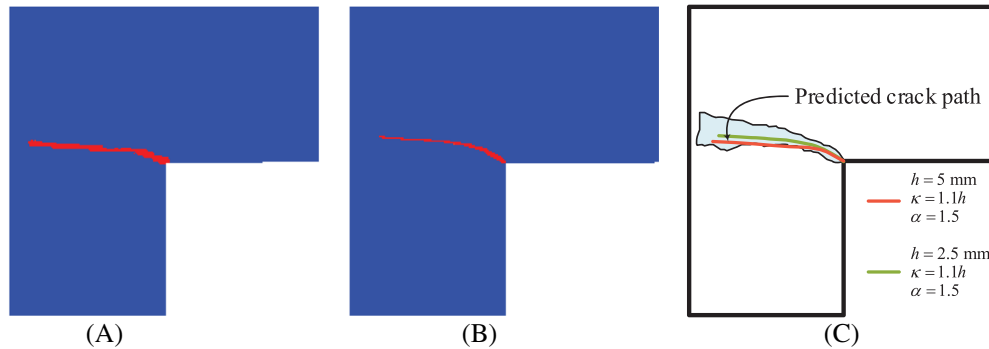
FIGURE 12 L-shaped panel test. Comparison of crack paths between simulation results: (A) $h = 5$ mm, $\kappa = 1.1\,h$, $\alpha = 1.5$; (B) $h = 2.5$ mm, $\kappa = 1.1\,h$, $\alpha = 1.5$; (C) experimentally observed crack pattern envelope and predicted crack paths [Color figure can be viewed at wileyonlinelibrary.com]

previous literature are not exactly the same. In the present study, we use the same problem setting as those in previous studies.[30,53,54] The brittle material considered is soda-lime glass, and its properties are $E = 72$ GPa, $\upsilon = 0.22$, $G_c = 135$ N/m, and $\rho = 2440$ kg/m^3. A constant traction load $\sigma_0 = 12$ MPa is applied at the top and bottom edge of the plate.

As discussed in Section 5.1, numerical results are insensitive to the discretization size, provided the size is sufficiently refined. Therefore, the discretization convergence analysis will no longer be performed in this example. With regard to simulation parameters, we only assess the influence of the neighborhood size κ while keeping the normalizing constant α unchanged. Specifically, three cases are considered: Case (1) for $\alpha = 2.0$ and $\kappa = 1.05\,h$; Case (2) for $\alpha = 2.0$ and $\kappa = 1.1\,h$; and Case (3) for $\alpha = 2.0$ and $\kappa = 1.15\,h$. In all simulations, the computational domain is discretized into 256 000 uniform particles with the background grid size $h = 0.25$ mm. The thickness of the plate is taken as the unit length h. To ensure accurate results, the time step is chosen to be 10^{-2} μs, which is smaller than the critical time step. In addition, the pre-existing crack is modeled using the phantom-node method (see Section 3.3.1), allowing the intact plate to be separated from the middle.

The crack evolution of the plate predicted with Case (2) at different times is shown in Figure 15. As can be observed, crack initiation occurs at approximately 12 μs due to the accumulation of elastic strain energy around the preexisting crack tip. The crack then grows horizontally until branching occurs at approximately 32 μs; after that, the crack propagates along two bifurcation paths until the plate is completely fractured at 68 μs.

Figure 16 shows the final numerical results for each case. As can be seen, the crack paths are similar for all the selected κ. This implies that the neighborhood size value within an appropriate range can give a relatively stable result such that we do not need to spend too much time to tune parameters. This characteristic is quite important for numerical simulations. Furthermore, the major features of the crack morphology observed in the simulations also agree well with other simulations in the literature.[30,53,54]

To further compare the global responses of the proposed model under the three cases, the energies as well as crack tip speed are measured during the crack evolution. Specifically, the elastic strain energy and the dissipated fracture energy
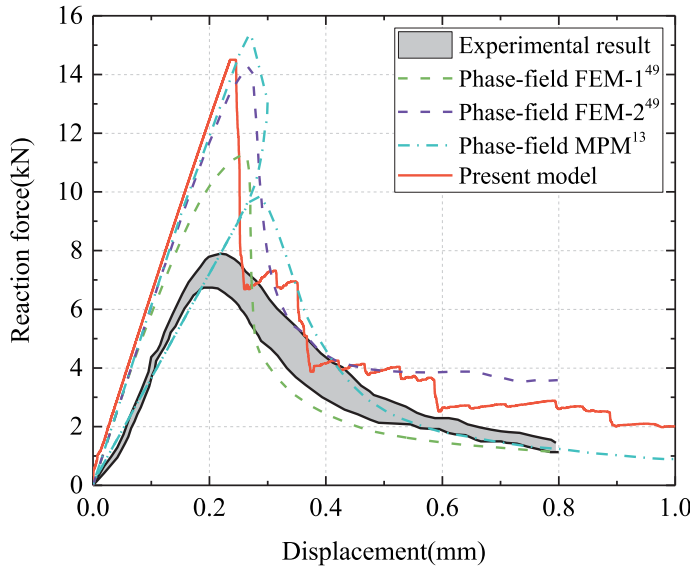
FIGURE 13 L-shaped panel test. Load-displacement curves from different numerical modeling and the experimental test [Color figure can be viewed at wileyonlinelibrary.com]
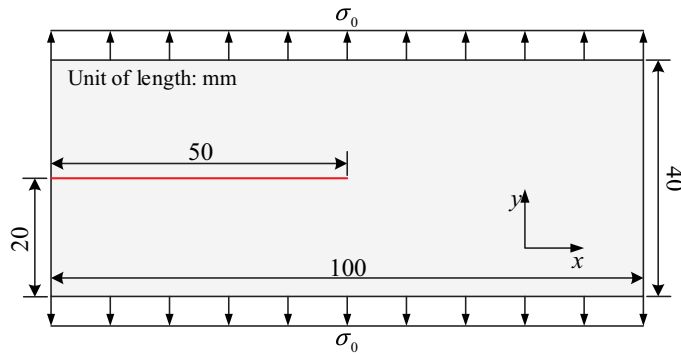

FIGURE 14 The geometry and boundary conditions for the crack branching example [Color figure can be viewed at wileyonlinelibrary.com]

are respectively, defined as

$$\Psi_e = \int_{\Omega\backslash A} \{c_p\psi_e^+(\varepsilon) + \psi_e^-(\varepsilon)\}\mathrm{d}\Omega = \sum_{p=1}^{n_p} \{c_p\psi_e^+(\varepsilon) + \psi_e^-(\varepsilon)\}V_p, \tag{32}$$

$$\Psi_f = \mathrm{G_c}\frac{|C_\kappa|}{2\kappa} = \frac{\mathrm{G_c}}{2\kappa}\sum_{p=1}^{n_e} V_p, \tag{33}$$

where n_e denotes the number of the eroded particles.

The computed energies including the elastic strain energy and the energy dissipated by the formation of the crack are plotted in Figure 17. As observed, the dissipated energy is underestimated for Case 3 by about 11% compared with Case 1 and Case 2. This underestimated fracture energy is manifested in the crack morphology with a relatively flat branching angle (see Figure 16). However, despite the differences, all cases can capture the satisfactory crack branching paths.

Figure 18 shows the simulated crack tip speed and the maximum speed (1580 m/s) obtained by experiment[55] for the soda-lime glass material. As can be seen, the simulated crack tip speed in Case 1 and Case 2 both stay well below the experimental maximum crack speed, and only in Case 3, the maximum speed is exceeded by 2.9%. These crack speed profiles are also close to the results obtained by the peridynamics method, as reported in References 53,54. Notably, the crack speed we obtain is slower than that obtained in References 53,54. This phenomenon is attributed to the neighboring-averaged operation on particles for the calculation of energy release rate. The energy at the crack tip is most released. However, after being averaged in the κ-neighborhood, the actual energy release rate at the tip decreases so that the crack propagation slows down. By contrast, because the damage field changes its value

FIGURE 15 Crack propagation predicted by the proposed approach in Case (2) [Color figure can be viewed at wileyonlinelibrary.com]
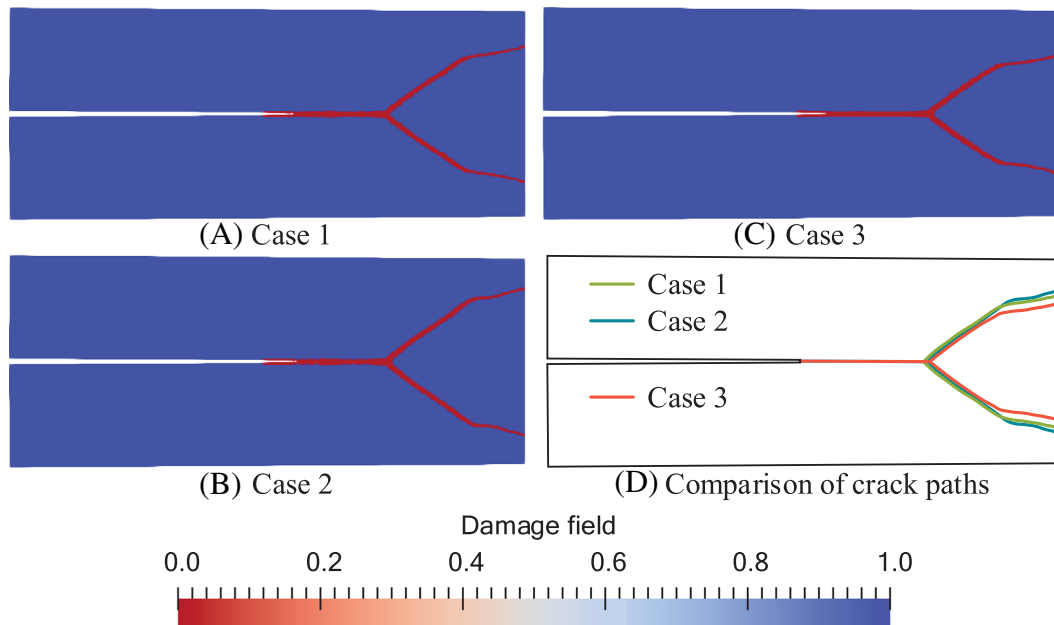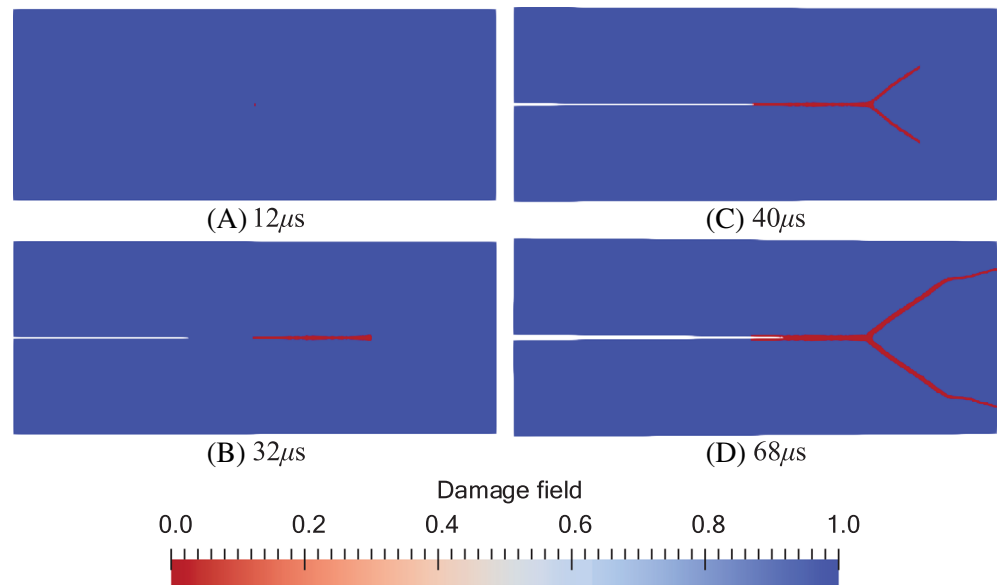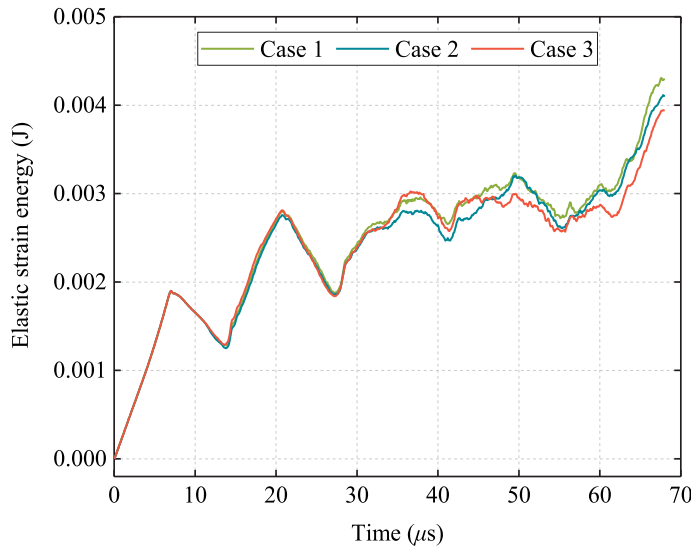

(A) $12\mu s$

(C) $40\mu s$

(B) $32\mu s$

(D) $68\mu s$

Damage field

0.0   0.2   0.4   0.6   0.8   1.0

(A) Case 1

(C) Case 3

(B) Case 2

(D) Comparison of crack paths

Damage field

0.0   0.2   0.4   0.6   0.8   1.0

FIGURE 16 Results for the crack branching example at $t = 68\,\mu s$ for the three cases [Color figure can be viewed at wileyonlinelibrary.com]

in a binary sense rather than in a continuous range, the material is either intact or completely damaged. Therefore, the intermediate damage state of the material is neglected such that the sustained damage effect on the material is reduced to a certain extent. Consequently, the formation of cracks becomes slower. We feel that the nongradual failure of material would be addressed by a continuous damage field as is commonly used in the phase-field fracture theory.

5.3 | Edge-cracked plate under impulsive loading

This example deals with the Kalthoff's experiment[56] in which a double prenotched steel plate is impacted by a projectile. Under the impact, the plate is subjected to dynamic shear loads, which eventually results in mode II cracks. Given the

FIGURE 17 Plots over time of energies, as defined by Equations (32) and (33) [Color figure can be viewed at wileyonlinelibrary.com]

(A) Stored elastic strain energy

(B) Dissipated fracture energy

symmetry of the configuration, only half of the plate is considered, as shown in Figure 19. The impact loading is imposed on the left edge by applying the kinematic velocity

$$v = \begin{cases} \frac{t}{t_0} v_0 & t \le t_0 \\ v_0 & t > t_0 \end{cases} \tag{34}$$

with $v_0 = 16.5$ m/s and $t_0 = 1$ μs. A symmetry condition is applied on the bottom of the plate, and the other edges are considered to be free boundaries. The material properties are taken from Borden et al[12]: $E = 190$ GPa, $v = 0.3$, $G_c = 22\,130$ N/m, and $\rho = 8000$ kg/m^3. The corresponding Rayleigh wave speed is $v_R = 2803$ m/s. The computational domain is discretized into 160 000 uniformly distributed material particles with a background grid size $h = 0.5$ mm. The notch is introduced in the background grid by the proposed phantom-node method. In the numerical simulation, the time step is set to 10^{-2} μs. The normalizing constant and neighborhood size are chosen to be $\alpha = 2.0$ and $\kappa = 1.15\,h$.

The temporal evolution of the crack is shown in Figure 20. As can be seen, the crack begins to propagate at approximately 26 μs, and then, grows at a large angle (about 70.5°) to about 40 μs, after which the angle decreases until the crack penetrates the plate at 102 μs. This crack pattern coincides with those obtained in previous studies.[7,12,52] The overall crack inclination angle is 66.5°, which agrees well with the experimental results where a brittle crack path with a propagation

FIGURE 18   Comparison of the crack tip propagation speed [Color figure can be viewed at wileyonlinelibrary.com]
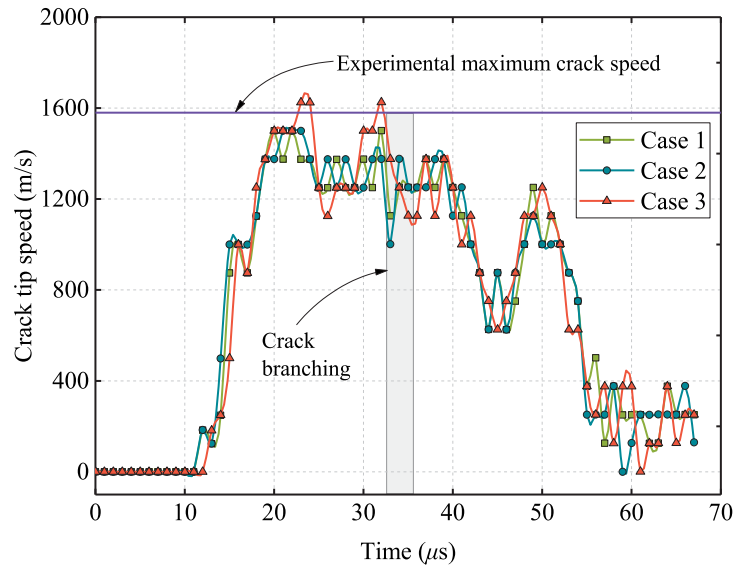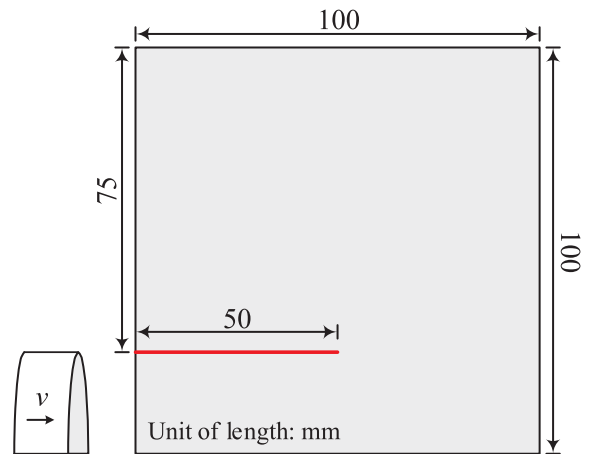

FIGURE 19   Geometry and boundary conditions for the edge-cracked plate example [Color figure can be viewed at wileyonlinelibrary.com]

angle of about 70° is observed. Figure 21 depicts the final crack trajectory obtained by different approaches. The speed of the crack tip is plotted in Figure 22. As observed, the maximum crack tip speed is 1635 m/s, which is smaller than 60% of the Rayleigh wave speed. A similar finding is reported by Borden et al.[12] These satisfactory results demonstrate the ability of the proposed EigenMPM in dealing with mode-II crack propagation problems.

Note that the present curve of crack speed is somewhat oscillatory. The oscillation is always encountered in MPM and is mainly caused by explicit schemes as well as the loss of information when transferring between particle and grid representations.[57] However, this problem can be addressed by advanced approaches, such as the affine particle-in-cell method,[57,58] the polynomial particle-in-cell method,[59] the XPIC(m) method,[60] and the null-space filter method.[61] Notably, although oscillation occurs, the results can always be acceptable. This is because opposite oscillations coexist that may contradict each other during the simulation process. Therefore, smooth displacement fields as well as energy fields can always be obtained. However, in the future, we will seek to further improve the proposed EigenMPM to better describe the failure behavior of materials.

5.4 | John-Shah test

The last benchmark concerns a three-point-bending beam test performed by John and Shah.[62] The test setup is shown in Figure 23, where a notch is preset at the bottom of the beam. The location of the notch is described by a parameter $\gamma = l_2/l_1$. By changing the position of the notch, two different crack modes can be observed in the experiment. Interestingly, a "transition point" γ_t was found, at which the crack propagation shifted from the offset notch to the midspan. For $\gamma < \gamma_t$,
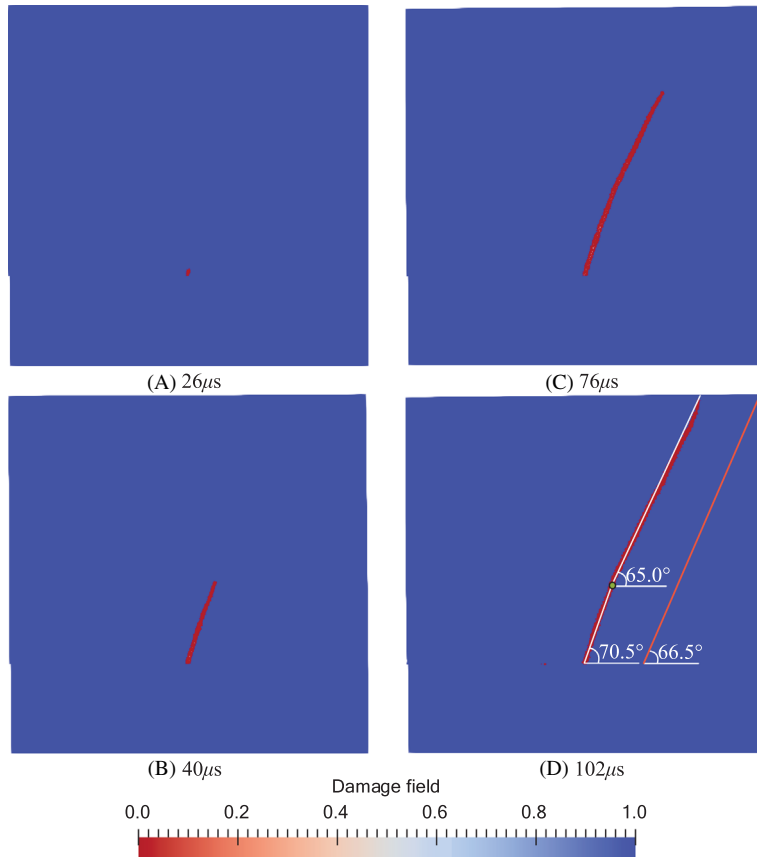
FIGURE 20 Temporal evolution of the crack in the edge-cracked plate [Color figure can be viewed at wileyonlinelibrary.com]

(A) 26μs (C) 76μs (B) 40μs (D) 102μs

65.0° 70.5° 66.5°

Damage field
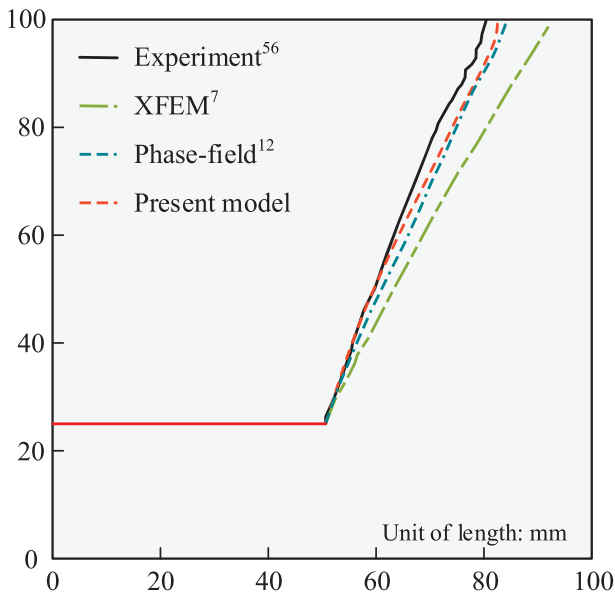0.0   0.2   0.4   0.6   0.8   1.0

FIGURE 21 Crack paths of Kalthoff's problem predicted by different numerical algorithms and experimental result [Color figure can be viewed at wileyonlinelibrary.com]

— Experiment[56]
—· XFEM[7]
-- Phase-field[12]
--· Present model

Unit of length: mm

a crack occurs at the notch; for $\gamma > \gamma_t$, a crack grows from the midspan. The test results show that for impact loading, $\gamma_t = 0.77$. Here, we seek to reproduce the crack modes using the proposed EigenMPM.

In the numerical simulations, the material properties are taken from the dynamic experiments: $E = 31.37$ GPa, $v = 0.2$, $G_c = 31.1$ N/m, and $\rho = 2400$ kg/m^3. The dynamic loading is simulated by applying a velocity boundary condition on the top point of the midspan. The impact velocity is imposed as References 52,63,64

$$v = \begin{cases} \frac{t}{t_0}v_0 & t \leq t_0 \\ v_0 & t > t_0 \end{cases} ,$$

(35)

FIGURE 22 Crack tip speed for the example of edge-cracked plate under impulsive loading [Color figure can be viewed at wileyonlinelibrary.com]
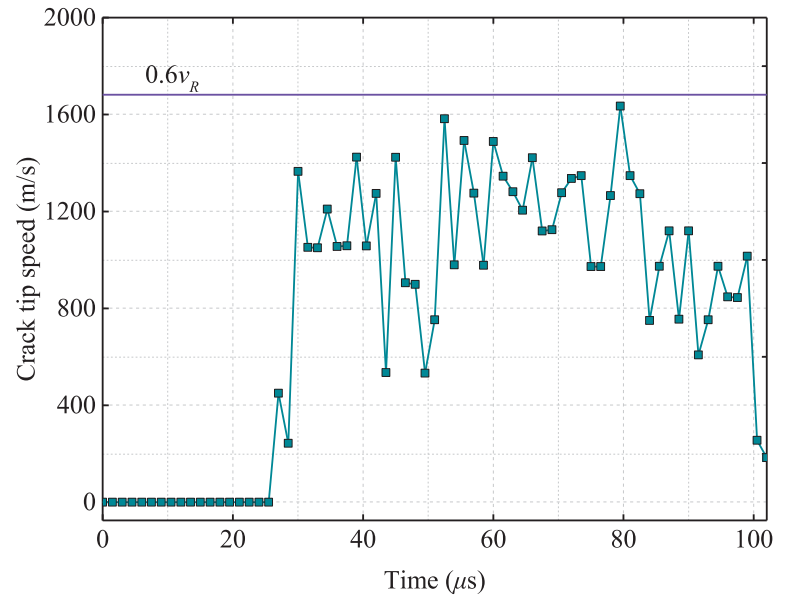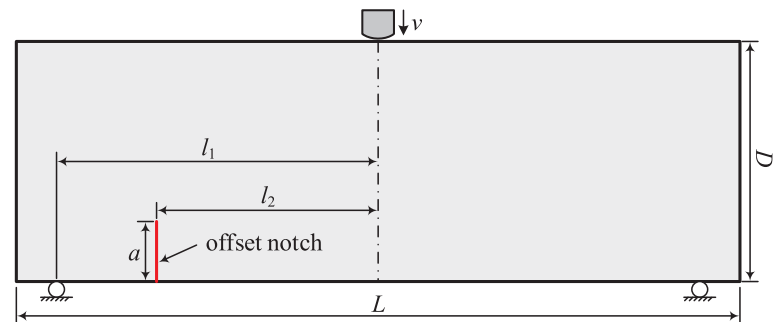

FIGURE 23 Geometry (Unit of length: mm) and loading condition of the John–Shah test, where D, L, l_1, and $a = 76.2$, 228.6, 101.6, and 19.05 (or 3, 9, 4, and 0.75 in), respectively [Color figure can be viewed at wileyonlinelibrary.com]

where $v_0 = 0.06$ m/s and $t_0 = 196$ μs.

The background grid size is set to $h = 0.635$ mm, and the thickness of the beam is assumed to be unit length h. To ensure accurate results, the time step is chosen to be 0.1 μs, which is smaller than the critical time step. The normalizing constant and neighborhood size are chosen to be $\alpha = 2.0$, $\kappa = 1.15\,h$. The offset notch is regarded as a preexisting crack. In addition, to represent the effect of a small flaw as well as to induce crack nucleation at the center, we refer to other research works[63,64] to place a small initial crack with a height of 1.27 mm (0.05 in) at the midspan.

The simulated crack patterns for different values of γ are shown in Figure 24. As can be seen, the feature that the transition of damage modes relies on the position of the notch is well captured. With the increase of γ from 0.5 to 0.75, crack initiation shifts from the notch to the midspan. The crack paths for $\gamma = 0.5$ and $\gamma = 0.72$ are close to those reported in the experiment.[62] Figure 25 shows the energy release rate of the beam for the case of $\gamma = 0.738$ and $\gamma = 0.744$. From the figure, we can observe that when the notch is far away from the midspan, the energy will be released more at the midspan than at the notch, which prompts the crack initiation to occur at the midspan first. This finally leads to different crack modes, as shown in Figure 24. Therefore, the "transition point" can be identified between 0.738 and 0.744, which matches well with the experimentally determined value of $\gamma_t = 0.77$. These findings reveal that the proposed EigenMPM can capture complex fracture modes.

6 | CONCLUSIONS

This work introduces an eigenerosion approach into the MPM framework (ie, EigenMPM) to deal with dynamic brittle fracture problems. Formulated within the variational theory, eigenerosion links the crack propagation to energy conservation. Compared with the widely used phase-field method, a major advantage of the EigenMPM is that the energy
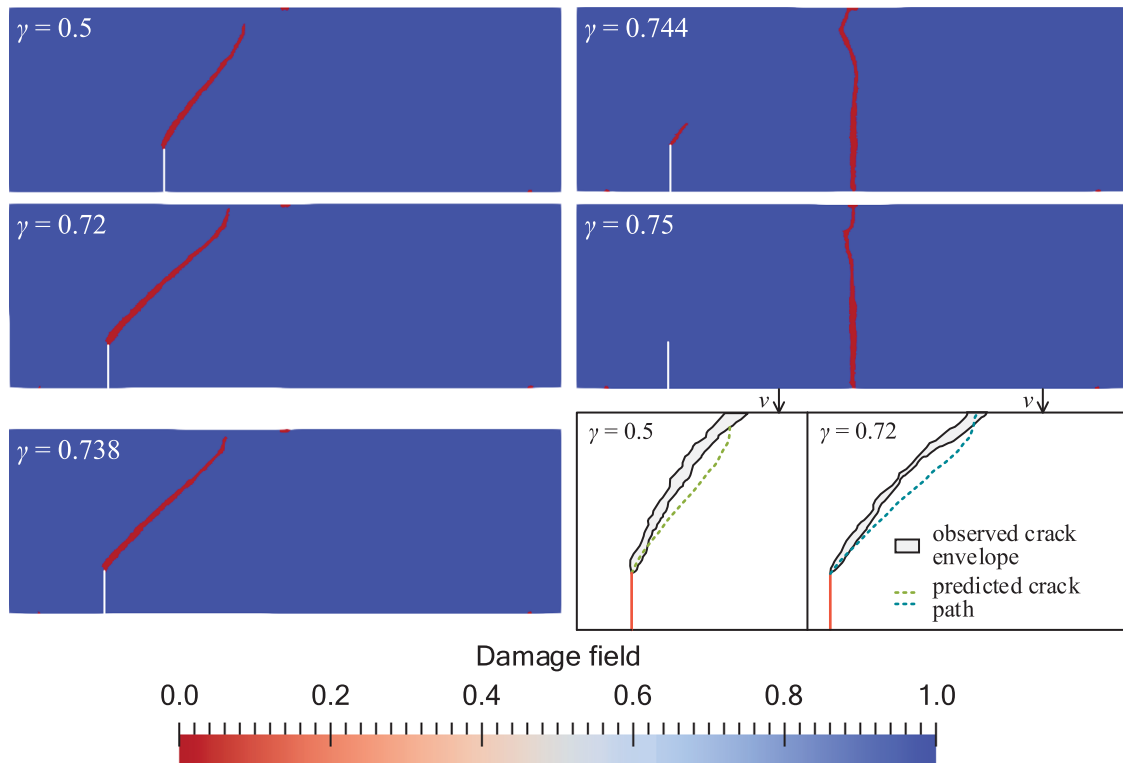
FIGURE 24   Simulated crack patterns for different values of γ and comparisons with the experimental results [Color figure can be viewed at wileyonlinelibrary.com]
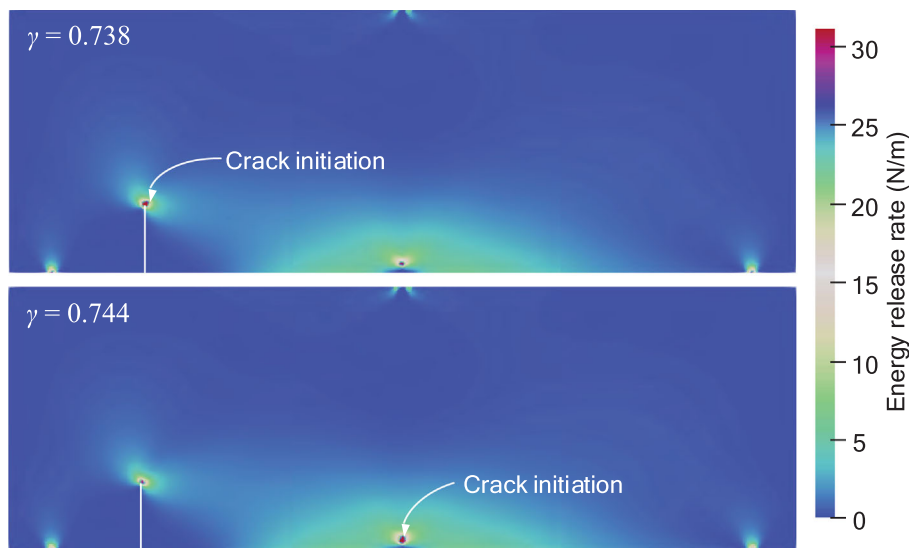

FIGURE 25   Energy release rate of the beam for the case of $\gamma = 0.738$ and $\gamma = 0.744$ [Color figure can be viewed at wileyonlinelibrary.com]

release rate of each particle that controls the crack propagation only needs to be calculated within its neighborhood domain. Moreover, the evaluation of the fracture behavior of a material can be decoupled from the governing equations as a separate solution step. Therefore, the eigenerosion scheme can be easily integrated into any standard MPM solver with minor modifications. One of the main advantages of the EigenMPM over other more elaborate models is that it adds little overhead to the existing computations.

Several representative benchmark tests for dynamic brittle fracture are presented to verify the proposed method. These examples demonstrate that EigenMPM can well predict complex dynamic fracture behaviors, including a mode-I crack, mode-II crack, bifurcating crack, and mixed-mode crack. Because two key parameters are embedded in the eigenerosion

approach, parametric studies are also conducted. Numerical investigations indicate that the normalizing constant only controls the initiation speed of the crack and has little effect on the final crack morphology, whereas the neighborhood size affects the crack pattern more. However, in our computational experience, when the value of the neighborhood size is between $1.0\,h$ and $1.25\,h$, satisfactory results can be obtained. In addition, a phantom-node method is proposed that allows for the cracks that initially existed in a solid body. This method only adds phantom nodes near the preexisting crack, which is proved to be effective by the examples.

While the proposed EigenMPM is capable of simulating cracks and has been validated against experimental and previous studies, there remain opportunities for further research. First, the current work mainly focuses on the linear elastic analysis, and the model cannot be applied to materials with viscoplastic behaviors. Therefore, it would be meaningful to include more realistic material constitutive models to simulate ductile and cohesive fracture. Second, conventional MPM/GIMP always faces stress oscillations. Although this does not substantially affect the final crack morphology, accurate fracture parameters are still needed because they are important to further understand the mechanical behavior of materials.

ACKNOWLEDGEMENTS

CONFLICT OF INTEREST
The authors declare that they have no conflict of interest.

ORCID
Shui-Long Shen https://orcid.org/0000-0002-5610-7988
Annan Zhou https://orcid.org/0000-0001-5209-5169

REFERENCES
1. Griffith AA. The phenomena of rupture and flow in solids. *Philos Trans R Soc Lond A*. 1921;221(2):163-198.
2. Song J-H, Belytschko T. Cracking node method for dynamic fracture with finite elements. *Int J Numer Methods Eng*. 2009;77(3):360-385.
3. Belytschko T, Fish J, Engelmann BE. A finite element with embedded localization zones. *Comput Methods Appl Mech Eng*. 1988;70(1):59-89.
4. Armero F, Linder C. Numerical simulation of dynamic fracture using finite elements with embedded discontinuities. *Int J Fract*. 2009;160(2):119-141.
5. Belytschko T, Black T. Elastic crack growth in finite elements with minimal remeshing. *Int J Numer Methods Eng*. 1999;45(5):601-620.
6. Moës N, Dolbow J, Belytschko T. A finite element method for crack growth without Remeshing. *Int J Numer Methods Eng*. 1999;46(1):131-150.
7. Song JH, Wang H, Belytschko T. A comparative study on finite element methods for dynamic fracture. *Comput Mech*. 2008;42(2):239-250.
8. Rabczuk T, Zi G, Gerstenberger A, Wall WA. A new crack tip element for the phantom-node method with arbitrary cohesive cracks. *Int J Numer Methods Eng*. 2008;75(5):577-599.
9. Turon A, Davila CG, Camanho PP, Costa J. An engineering solution for mesh size effects in the simulation of delamination using cohesive zone models. *Eng Fract Mech*. 2007;74(10):1665-1682.
10. Elices M, Guinea G, Gomez J, Planas J. The cohesive zone model: advantages, limitations and challenges. *Eng Fract Mech*. 2002;69(2):137-163.
11. Ren H, Zhuang X, Anitescu C, Rabczuk T. An explicit phase field method for brittle dynamic fracture. *Comput Struct*. 2019;217:45-56.
12. Borden MJ, Verhoosel CV, Scott MA, Hughes TJ, Landis CM. A phase-field description of dynamic brittle fracture. *Comput Methods Appl Mech Eng*. 2012;217:77-95.
13. Kakouris E, Triantafyllou SP. Phase-field material point method for brittle fracture. *Int J Numer Methods Eng*. 2017;112(12):1750-1776.
14. Wolper J, Fang Y, Li M, Lu J, Gao M, Jiang C. CD-MPM: continuum damage material point methods for dynamic fracture animation. *ACM Trans Graph*. 2019;38(4):1-15.
15. Cervera M, Chiumenti M. Mesh objective tensile cracking via a local continuum damage model and a crack tracking technique. *Comput Methods Appl Mech Eng*. 2006;196(1–3):304-320.
16. Saloustros S, Pelà L, Cervera M, Roca P. Finite element modelling of internal and multiple localized cracks. *Comput Mech*. 2017;59(2):299-316.
17. Karma A, Kessler DA, Levine H. Phase-field model of mode III dynamic fracture. *Phys Rev Lett*. 2001;87(4):045501.
18. Miehe C, Welschinger F, Hofacker M. Thermodynamically consistent phase-field models of fracture: Variational principles and multi-field FE implementations. *Int J Numer Methods Eng*. 2010;83(10):1273-1311.

19. Arriaga M, Waisman H. Stability analysis of the phase-field method for fracture with a general degradation function and plasticity induced crack generation. *Mech Mater*. 2018;116:33-48.

20. Wu JY, Nguyen VP. A length scale insensitive phase-field damage model for brittle fracture. *J Mech Phys Solids*. 2018;119:20-42.

21. Pandolfi A, Ortiz M. An eigenerosion approach to brittle fracture. *Int J Numer Methods Eng*. 2012;92(8):694-714.

22. Jiang H, Jiang F, Hu D, Wang R, Lu J, Li B. Numerical modeling of compressive failure mechanisms in ceramic materials at high strain rates. *Comput Methods Appl Mech Eng*. 2019;347:806-826.

23. Schmidt B, Fraternali F, Ortiz M. Eigenfracture: an eigendeformation approach to variational fracture. *Multiscale Model Simul*. 2009;7(3):1237-1266.

24. Pandolfi A, Li B, Ortiz M. Modeling fracture by material-point erosion. *Int J Fract*. 2013;184(1–2):3-16.

25. Li B, Pandolfi A, Ortiz M. Material-point erosion simulation of dynamic fragmentation of metals. *Mech Mater*. 2015;80:288-297.

26. Stochino F, Qinami A, Kaliske M. Eigenerosion for static and dynamic brittle fracture. *Eng Fract Mech*. 2017;182:537-551.

27. Belytschko T, Gu L, Lu Y. Fracture and crack growth by element free Galerkin methods. *Model Simul Mater Sci Eng*. 1994;2(3A):519-534.

28. Batra R, Zhang G. Search algorithm, and simulation of elastodynamic crack propagation by modified smoothed particle hydrodynamics (MSPH) method. *Comput Mech*. 2007;40(3):531-546.

29. Pramanik R, Douillet-Grellier T, Pan K, Jones BD. An SPH approach to the simulation of hydraulic fracture propagation in naturally fractured rock medium. Paper presented at: ARMA 50th US Rock Mechanics/Geomechanics Symposium; 2016.

30. Ha YD, Bobaru F. Studies of dynamic crack propagation and crack branching with peridynamics. *Int J Fract*. 2010;162(1–2):229-244.

31. Shojaei A, Mossaiby F, Zaccariotto M, Galvanetto U. An adaptive multi-grid peridynamic method for dynamic fracture analysis. *Int J Mech Sci*. 2018;144:600-617.

32. Liang Y, Benedek T, Zhang X, Liu Y. Material point method with enriched shape function for crack problems. *Comput Methods Appl Mech Eng*. 2017;322:541-562.

33. Sulsky D, Chen Z, Schreyer HL. A particle method for history-dependent materials. *Comput Methods Appl Mech Eng*. 1994;118(1–2):179-196.

34. Nairn JA. Material point method calculations with explicit cracks. *CMES-Comp Model Eng Sci*. 2003;4(6):649-664.

35. Guo Y, Nairn J. Three-dimensional dynamic fracture analysis using the material point method. *CMES-Comp Model Eng Sci*. 2006;16(3):141.

36. Guo Y, Nairn J. Simulation of dynamic 3D crack propagation within the material point method. *CMES-Comp Model Eng Sci*. 2017;113(4):389-410.

37. Chen Z, Shen L, Mai YW, Shen YG. A bifurcation-based decohesion model for simulating the transition from localization to decohesion with the MPM. *Z Angew Math Phys*. 2005;56(5):908-930.

38. Sulsky D, Schreyer L. MPM simulation of dynamic material failure with a decohesion constitutive model. *Eur J Mech A-Solids*. 2004;23(3):423-445.

39. Yang P, Gan Y, Zhang X, Chen Z, Qi W, Liu P. Improved decohesion modeling with the material point method for simulating crack evolution. *Int J Fract*. 2014;186(1–2):177-184.

40. Francfort GA, Marigo J-J. Revisiting brittle fracture as an energy minimization problem. *J Mech Phys Solids*. 1998;46(8):1319-1342.

41. Liang Y, Zhang X, Liu Y. An efficient staggered grid material point method. *Comput Methods Appl Mech Eng*. 2019;352:85-109.

42. Bardenhagen SG, Kober EM. The generalized interpolation material point method. *CMES-Comp Model Eng Sci*. 2004;5(6):477-496.

43. Wallstedt PC, Guilkey J. An evaluation of explicit time integration schemes for use with the generalized interpolation material point method. *J Comput Phys*. 2008;227(22):9628-9642.

44. Zhang X, Chen Z, Liu Y. *The Material Point Method: A Continuum-Based Particle Method for Extreme Loading Cases*. Cambridge, MA: Academic Press; 2016.

45. Navas P, Rena CY, Li B, Ruiz G. Modeling the dynamic fracture in concrete: an eigensoftening meshfree approach. *Int J Impact Eng*. 2018;113:9-20.

46. Allen MP, Tildesley DJ. *Computer Simulation of Liquids*. Oxford: Oxford University Press; 2017.

47. Bardenhagen S. Energy conservation error in the material point method for solid mechanics. *J Comput Phys*. 2002;180(1):383-403.

48. Winkler BJ. *Traglastuntersuchungen von unbewehrten und bewehrten Betonstrukturen auf der Grundlage eines objektivenWerkstoffgesetzes für Beton*. Innsbruck: University of Innsbruck; 2001.

49. Zhang X, Vignes C, Sloan SW, Sheng D. Numerical evaluation of the phase-field model for brittle fracture with emphasis on the length scale. *Comput Mech*. 2017;59(5):737-752.

50. Belytschko T, Chen H, Xu J, Zi G. Dynamic crack propagation based on loss of hyperbolicity and a new discontinuous enrichment. *Int J Numer Methods Eng*. 2003;58(12):1873-1905.

51. Xu D, Liu Z, Liu X, Zeng Q, Zhuang Z. Modeling of dynamic crack branching by enhanced extended finite element method. *Comput Mech*. 2014;54(2):489-502.

52. Nguyen VP, Wu JY. Modeling dynamic fracture of solids with a phase-field regularized cohesive zone model. *Comput Methods Appl Mech Eng*. 2018;340:1000-1022.

53. Dipasquale D, Zaccariotto M, Galvanetto U. Crack propagation with adaptive grid refinement in 2D peridynamics. *Int J Fract*. 2014;190(1–2):1-22.

54. Bie Y, Cui X, Li Z. A coupling approach of state-based peridynamics with node-based smoothed finite element method. *Comput Methods Appl Mech Eng*. 2018;331:675-700.

55. Bowden F, Brunton J, Field J, Heyes A. Controlled fracture of brittle solids and interruption of electrical current. *Nature*. 1967;216(5110):38-42.

56. Kalthoff JF. Modes of dynamic shear failure in solids. *Int J Fract.* 2000;101(1–2):1-31.
57. Jiang C, Schroeder C, Selle A, Teran J, Stomakhin A. The affine particle-in-cell method. *ACM Trans Graph.* 2015;34(4):1-10.
58. Jiang C, Schroeder C, Teran J. An angular momentum conserving affine-particle-in-cell method. *J Comput Phys.* 2017;338:137-164.
59. Fu C, Guo Q, Gast T, Jiang C, Teran J. A polynomial particle-in-cell method. *ACM Trans Graph.* 2017;36(6):1-12.
60. Hammerquist CC, Nairn JA. A new method for material point method particle updates that reduces noise and enhances stability. *Comput Methods Appl Mech Eng.* 2017;318:724-738.
61. Tran QA, Sołowski W. Temporal and null-space filter for the material point method. *Int J Numer Methods Eng.* 2019;120(3):328-360.
62. John R, Shah SP. Mixed-mode fracture of concrete subjected to impact loading. *J Struct Eng.* 1990;116(3):585-602.
63. Belytschko T, Organ D, Gerlach C. Element-free Galerkin methods for dynamic fracture in concrete. *Comput Methods Appl Mech Eng.* 2000;187(3–4):385-399.
64. Zi G, Chen H, Xu J, Belytschko T. The extended finite element method for dynamic fractures. *Shock Vib.* 2005;12(1):9-23.

SUPPORTING INFORMATION

Additional supporting information may be found online in the Supporting Information section at the end of this article.

APPENDIX A. ESTIMATION FOR THE NEIGHBORHOOD SIZE

According to Li et al,[25] the neighborhood size κ can be set as

$$\kappa = \lambda r \tag{A1}$$

in the optimal transportation meshfree method, where r is the numerical size of the particle and λ is a constant. The size r can be estimated as

$$r = \sqrt[1/d]{d!V} \tag{A2}$$

where d and V indicate the dimension of the problem and the volume of the particle, respectively. For an MPM procedure where the initial particle size is half of the background grid size h, r is reduced to $r = 0.5 \sqrt[1/d]{d!}h$. The constant λ can be chosen between 1.0 and 2.0. Then, the neighborhood size κ can be set using the following equation:

$$\kappa \in \begin{cases} \left[0.5\sqrt{2}h, \sqrt{2}h \right], & \text{for 2D problems} \\ \left[0.5 \sqrt[1/3]{6}h, \sqrt[1/3]{6}h \right], & \text{for 3D problems} \end{cases} \tag{A3}$$

Equation (A3) establishes an estimated relationship between the neighborhood size κ and the background grid size h. Once h is determined, κ can be estimated according to Equation (A3).